Title: A basally active cGAS-STING pathway limits SARS-CoV-2 replication in a subset of ACE2 positive airway cell models

Maritza Puray-Chavez[1], Jenna E. Eschbach[1], Ming Xia[1], Kyle M. LaPak[2], Qianzi Zhou[1], Ria Jasuja[2], Jiehong Pan[3], Jian Xu[3], Zixiang Zhou[1], Shawn Mohammed[1], Qibo Wang[1], Dana Q. Lawson[1], Sanja Djokic[1], Gaopeng Hou[1], Siyuan Ding[1], Steven L. Brody[3], Michael B. Major[2,4], Dennis Goldfarb[2,5], Sebla B. Kutluay[1,*]

[1]Department of Molecular Microbiology, Washington University School of Medicine, St. Louis, MO, USA

[2]Department of Cell Biology and Physiology, Washington University School of Medicine, St. Louis, MO, USA

[3]Division of Pulmonary and Critical Care Medicine, Department of Medicine, Washington University School of Medicine, St. Louis, MO, USA

[4]Department of Otolaryngology, Washington University School of Medicine, St. Louis, MO, USA

[5]Institute for Informatics, Data Science & Biostatistics, Washington University School of Medicine, St. Louis, MO, USA.

Running title: Basally active cGAS-STING limits SARS-CoV-2 infection

*Correspondence: kutluay@wustl.edu (S.B.K.)

ABSTRACT

Host factors that define the cellular tropism of SARS-CoV-2 beyond the cognate ACE2 receptor are poorly defined. Here we report that SARS-CoV-2 replication is restricted at a post-entry step in a number of ACE2-positive airway-derived cell lines due to tonic activation of the cGAS-STING pathway mediated by mitochondrial DNA leakage and naturally occurring cGAS and STING variants. Genetic and pharmacological inhibition of the cGAS-STING and type I/III IFN pathways as well as ACE2 overexpression overcome these blocks. SARS-CoV-2 replication in STING knockout cell lines and primary airway cultures induces ISG expression but only in uninfected bystander cells, demonstrating efficient antagonism of the type I/III IFN-pathway in productively infected cells. Pharmacological inhibition of STING in primary airway cells enhances SARS-CoV-2 replication and reduces virus-induced innate immune activation. Together, our study highlights that tonic activation of the cGAS-STING and IFN pathways can impact SARS-CoV-2 cellular tropism in a manner dependent on ACE2 expression levels.

42 **INTRODUCTION**

43 Severe acute respiratory syndrome coronavirus 2 (SARS-CoV-2) is continuing to cause significant
44 respiratory disease and mortality in vulnerable populations. The emergence of highly
45 transmissible viral variants resistant to vaccines and existing immunity is an ongoing concern.
46 The innate immune response mediated by type I, type II and type III interferons (IFNs) constitutes
47 a potent block to SARS-CoV-2 replication [1-3]. It remains unknown if IFN-mediated antiviral
48 responses can modulate the cellular tropism of SARS-CoV-2 independently of the cognate host
49 cell SARS-CoV-2 receptor, angiotensin converting enzyme 2 (ACE2). Given the multiple ways in
50 which SARS-CoV-2 can antagonize IFN production and signaling [1-3], a comprehensive
51 understanding of the interplay between these mechanisms may inform the observed multi-organ
52 involvement, reveal new facets of emerging SARS-CoV-2 variants and ultimately identify new
53 opportunities for therapeutic intervention.

54 SARS-CoV-2 homotrimeric spike (S) glycoprotein binding to the host cell ACE2 receptor mediates
55 viral entry [4-7]. Endogenous ACE2 expression is surprisingly low in the respiratory tract [8,9]
56 compared with higher levels in other tissues of the gastrointestinal tract, kidney and myocardium
57 [10,11]. Although ectopic expression of ACE2 is sufficient for viral entry in several cell culture and
58 animal models [4-7,12], additional factors and host cell proteases including TMPRSS2 may contribute
59 to defining the cellular tropism of SARS-CoV-2 (and variants thereof) at physiological levels of
60 ACE2 expression [13]. Growing evidence suggests that viral attachment factors can facilitate ACE2-
61 dependent and even enable ACE2-independent entry [13,14]. Together, these alternative receptors
62 and attachment factors may compensate for the low levels of ACE2 expression in various organs,
63 including the distal respiratory system.

64 In addition to the identity and expression of entry factors and receptors, SARS-CoV-2 cellular
65 tropism can in principle be determined by the basal activation of cell intrinsic and innate immune

66 defenses that are canonically mounted in response to pathogens. For example, a preactivated
67 antiviral innate immunity in the upper airways of young children has been proposed to limit SARS-
68 CoV-2 replication [15]. In addition, healthy microbiota and endogenous retrovirus activation can also
69 promote antiviral innate immunity through cGAS/STING and subsequent type I/III IFN pathway
70 activation [16-21]. Interestingly, disruptions in microbiota homeostasis in both the respiratory and the
71 gastrointestinal tracts, the primary targets of SARS-CoV-2 [22-25], have been observed in
72 hospitalized COVID-19 patients [26-30] highlighting a possible link between basal innate immune
73 activation and SARS-CoV-2 pathogenesis.

74 Given the potent antiviral effects of type I/III IFNs, numerous SARS-CoV-2 encoded proteins have
75 evolved to antagonize IFN synthesis or subsequent IFN signaling pathways to allow efficient viral
76 spread [1-3]. On the other hand, we and others have shown that the RIG-I-like receptors (RLRs),
77 RIG-I and MDA5, can detect SARS-CoV-2 replication intermediates [31-37], resulting in robust, albeit
78 possibly delayed IFN-dependent innate immune activation [38-42]. Of note, severe COVID-19
79 patients also exhibit an impaired type I and III IFN response but a heightened inflammatory
80 response [43,44] in part due to the presence of autoantibodies against type I IFNs [45]. Similarly, young
81 infants exhibit restrained IFN-γ production following SARS-CoV-2 infection compared to adults [46].
82 Given these multifactorial antagonistic relationships between SARS-CoV-2 and host cells, cell
83 and tissue tropism and subsequent pathogenesis of SARS-CoV-2 is plausibly shaped by a
84 complex interplay of receptor presence and expression levels, innate immune activation state of
85 the target cells and distinct viral proteins that antagonize the host cell antiviral responses.

86 In this work, we sought to understand the molecular basis of an intrinsic resistance to SARS-CoV-
87 2 replication in a panel of lung and upper airway cell lines expressing comparably high levels of
88 endogenous ACE2/TMPRSS2[31] (from herein referred to as ACE2(high)). Analysis of the
89 transcriptomic signatures of 10 airway-derived cell lines reveal markedly higher levels of ISGs
90 and IFN pathway mediators in the ACE2(high) cells. A targeted genetic screen in a representative

91 ACE2(high) cell line reveals that the constitutive activation of the cGAS-STING pathway underlies
92 the observed IFN pathway activity. Genetic disruption and pharmacological inhibition of the cGAS-
93 STING and IFN pathways substantially decrease baseline ISG expression and enhance virus
94 replication in multiple ACE2(high) cell lines. We demonstrate that the basal cGAS-STING pathway
95 activity in these cells is likely maintained by a combination of mitochondrial DNA (mtDNA) leakage
96 and naturally occuring cGAS/STING variants that are more prone to activation. ACE2
97 overexpression efficiently overcomes the IFN-mediated blocks to SARS-CoV-2 replication,
98 demonstrating the ability of SARS-CoV-2 to overcome these possibly saturable post-entry blocks
99 to infection. SARS-CoV-2 replication in STING knockout cells and in primary human airway
100 cultures triggers type I IFN pathway activation, but only in uninfected bystander cells, suggesting
101 efficient antagonism of the IFN signaling pathway in infected cells. Furthermore, in primary human
102 airway cultures SARS-CoV-2-infected cells display markedly lower levels of STING expression
103 and pharmacological inhibition of STING enhances infectious virion release while limiting innate
104 immune activation. Collectively our study highlights that basal activation of the cGAS-STING and
105 subsequent IFN pathways contribute to defining the SARS-CoV-2 cellular tropism *in vitro* in a
106 manner dependent on ACE2 expression levels. Our findings also establish a pivotal role for
107 STING in establishment of antiviral responses in the relevant airway infection models and expand
108 the culture models available to study CoV-host interactions.

109 **RESULTS**

110 ***SARS-CoV-2 replication is blocked at a post-entry stage in a subset of airway-derived cell***
111 ***lines that endogenously express ACE2.***

112 We previously screened 10 human lung and upper airway cell lines expressing variable levels of
113 endogenous ACE2/TMPRSS2 for their ability to support SARS-CoV-2 replication[31].
114 Unexpectedly, we found four cell models—SCC25, H596, OE21 and Detroit 562—that express

115 comparably higher levels of ACE2 mRNA (**Fig. S1a**) and protein but were resistant to SARS-CoV-
116 2 replication [31]. Of note, these initial screens were conducted with a SARS-CoV-2 stock carrying
117 the S E484D substitution, which arises consistently during cell culture adaptation and allows virus
118 replication in an ACE2-independent manner [31,47]. Given this possible complication, we first
119 validated the ability of virus stocks verified to bear wild type (WT) S to infect these ACE2
120 expressing cells. SARS-CoV-2 (2019-nCoV/USA-WA1/2020) WT S productively infected PC-9,
121 KYSE-30 and H1299 cells that express lower levels of ACE2 (**Fig. S1a**) in addition to the control
122 Calu-3 and HCC827 cells, as evident from the substantial increase in the amount of cell-
123 associated viral RNA (**Fig. 1a**), viral N antigen (**Fig. S1b**) and infectious virion release in cell
124 culture supernatants (**Fig. 1b**) following virus inoculation. CRISPR-mediated knockout of ACE2
125 decreased cell-associated SARS-CoV-2 RNA by ~20 to 4000-fold in these cells (**Fig. 1c**),
126 validating the ACE2-dependence of virus replication. In agreement with our prior findings [31],
127 ACE2(high) cell lines including SCC25, H596, OE21 and Detroit 562 were largely resistant to
128 SARS-CoV-2 replication (**Fig. 1a-c, S1b**). Importantly, we found that ACE2 knockout led to a
129 significant reduction in incoming cell-associated SARS-CoV-2 RNA in the ACE2(high) cell lines
130 (**Fig. 1d, e**), suggesting a post-binding and/or post-entry block to virus replication and spread.
131 These results demonstrate that ACE2 expression is not sufficient to allow productive SARS-CoV-
132 2 replication in the ACE2(high) SCC25, H596, OE21, and Detroit 562 cell lines.

133 ***ACE2(high) airway-derived cell lines express high baseline levels of IFN pathway genes***

134 A common block to SARS-CoV-2 replication is mediated by type I and type III IFNs [1-3], as
135 exemplified by potent inhibition of SARS-CoV-2 replication by IFN-α pretreatment of Calu-3 cells
136 (**Fig. S2a**). Seeking to understand if IFN pathway activity contributed to SARS-CoV-2 resistance
137 in the ACE2(high) SCC25, H596, OE21, and Detroit 562 cells, we first evaluated the expression
138 of IFN pathway response genes by using publicly available RNA-seq data. Strikingly,
139 transcriptomic signatures of the cell line panel revealed substantially higher basal expression

140 levels of numerous ISGs, IFN pathway components and inflammatory mediators (e.g. *CCL2*,
141 *CCL5*, *IL6*, *CXCL9*) in the ACE2(high) cells compared to those that express low to no ACE2 (**Fig.**
142 **2a**). RT-qPCR and immunoblotting confirmed this observation and showed markedly high
143 baseline expression of several ISGs and IFN-pathway mediators (i.e. MX1, IFIT1, STAT1,
144 pSTAT1, IRF7 and IRF9) in SCC25, H596 and OE21 cells, moderately higher levels of distinct
145 ISGs in Detroit 562 cells (**Fig. 2b-f, S2b, S2c**). Further investigation of the RNA-seq data revealed
146 elevated levels of type I and type III IFNs in the ACE2(high) SCC25, H596, OE21 but not Detroit
147 562 cells or those permissive to infection (**Fig. S2d**); however, the amount of IFN-β and IFN-λ
148 protein in cell culture supernatants was below the limit of detection in ELISA assays (**Fig. S2e**,
149 **S2f**). In addition to the basally high ISG levels and despite the lack of noticeable virus replication,
150 SCC25, H596, OE21 and Detroit 562 cells responded to SARS-CoV-2 inoculation by further
151 upregulation of ISGs (**Fig. 2g, 2h, S2g-j**). Collectively, these findings suggest that the basally high
152 levels of ISG expression, coupled with further elevation of ISGs upon SARS-CoV-2 inoculation,
153 may underlie the post-entry block to infection in the ACE2(high) SCC25, H596, OE21 and Detroit
154 562 cells.

155 ***Basally active type I/III IFN signaling pathway underlies the resistance of ACE2(high) cell***
156 ***lines to SARS-CoV-2 replication***

157 To evaluate whether the constitutive activity of the canonical type I/III IFN pathway underlies the
158 resistance of SCC25, H596, OE21 and Detroit 562 cells to SARS-CoV-2 infection, cells were
159 pretreated with ruxolitinib, a JAK1/2 inhibitor, and inoculated with SARS-CoV-2 in its presence.
160 Ruxolitinib pretreatment decreased the baseline expression of five canonical ISGs (*IFIT1*, *MX1,*
161 *IFIT2, ISG15* and *IRF9*) in SCC25 cells (**Fig. 3a, 3b, S3a-c**), though the effects were relatively
162 modest for certain ISGs. Subsets of these ISGs were also suppressed in the other ACE2(high)
163 cell models (**Fig. 3a, 3b, S3a-c**). Ruxolitinib treatment resulted in an approximate 3-log increase
164 in the amount of cell-associated SARS-CoV-2 RNA in OE21 and SCC25, but not in Detroit 562

165 or H596 cells (**Fig. 3c**). Because of this, we decided to focus our studies primarily on SCC25 cells
166 with validation experiments in OE21 cells. In agreement with the ruxolitinib data, CRISPR-
167 mediated knockout of IFNAR and STAT1 (**Fig. S3d**), and siRNA-mediated depletion of
168 downstream IFN pathway components STAT2 and IRF9 (**Fig. S3e, S3f**) enhanced SARS-CoV-2
169 replication in SCC25 cells (**Fig. 3d-G, S3g**). STAT1 knockout also increased cell-associated viral
170 RNA levels in OE21 and more modestly in Detroit 562 cells, whereas H596 cells remained
171 resistant to infection despite a reduction in ISG expression (**Fig. S3h-k**). Enhancement of SARS-
172 CoV-2 replication in SCC25 and OE21 cells correlated with a reduction in baseline ISG expression
173 (**Fig. S3l, S3m**), though we noted that expression of certain ISGs including *IFIT2* and *OASL* was
174 less sensitive to STAT1 depletion. Together, these data suggest that the high baseline activity of
175 the canonical type I/III IFN signaling underlies the inability of OE21, SCC25 and Detroit 562 cells
176 to support SARS-CoV-2 replication.

177 ***Tonic activation of the cGAS-STING pathway underlies the resistance of SCC25, OE21 and***
178 ***Detroit 562 cells to SARS-CoV-2 replication***

179 To identify the molecular basis of the basally high IFN pathway activity in the SCC25 cells, we
180 conducted an siRNA screen (2 siRNAs/target) targeting host cell factors involved in sensing of
181 virus replication intermediates including TLRs (e.g. TLR3, TLR7, TLR8 and TLR9), RLRs (e.g.
182 RIG-I, MDA5 and LGP2) as well as their downstream adaptor molecules (e.g. MyD88, TRIF and
183 MAVS), NOD-like receptor family members (i.e. NOD2, NLRP1, NLRP3 and NLRC5) and the
184 cytosolic DNA sensor STING. Remarkably, depletion of STING by two independent siRNAs
185 substantially increased (~2-3-logs) cell-associated viral RNA levels in SCC25 cells (**Fig. 4a**).
186 Although knockdown of other sensors and downstream adaptors by individual siRNAs increased
187 viral RNA levels up to 10-fold, effects were comparably modest and siRNA-specific (**Fig. 4a**).
188 Consistent with the screening results, CRISPR-mediated knockout of cGAS, STING as well as
189 downstream signaling molecules TBK1 and IRF3 significantly increased cell-associated viral RNA

190 and antigen levels in SCC25 (**Fig. 4b, 4c**) as well as OE21 cells (**Fig. S4a**). Constitutive cGAS-
191 STING pathway activity was also evident in the higher levels of phosphorylated STING and IRF3
192 present in SCC25 and OE21 cell lysates (**Fig. S4b**). STING knockout also enhanced SARS-CoV-
193 2 replication in the ACE2(high) Detroit 562 cells, whereas H596 cells remained resistant to
194 infection (**Fig. S4c, S4d**). Furthermore, STING knockout did not enhance virus replication further
195 in the otherwise permissive cells (**Fig. S4c, S4d**).

196 Despite the enhanced SARS-CoV-2 replication in STING KO SCC25 cells, we noted that virus
197 spread was limited at later time points in infection (**Fig. 4d, S4e**). Ruxolitinib treatment of STING
198 KO cells allowed greater virus spread (**Fig. 4e**), suggesting that SARS-CoV-2-induced innate
199 immune activation independent of STING limits viral spread. Interestingly, we found that the
200 repressive effects of the type I/III IFN pathway were overcome by ACE2 overexpression in
201 SCC25, OE21, H596 and Detroit 562 cells (**Fig. 4f**) and ruxolitinib treatment did not further
202 enhance virus replication (**Fig. S4f**). It has been reported that the VOCs are generally less
203 sensitive to the inhibitory effects of type I IFNs [48]. Ruxolitinib pretreatment enhanced virus
204 replication 2-3 logs in SCC25 cells for most of the VOCs with the exception of the Delta and Kappa
205 variant strains, which responded to ruxolitinib treatment only modestly, and the Omicron strain
206 which remained nonresponsive (**Fig. S4g**). We further evaluated whether the IFN-mediated
207 restriction of SARS-CoV-2 replication in SCC25 and OE21 cells was mediated by ISGs known to
208 restrict SARS-CoV-2 replication [49-51] through a targeted siRNA screen. While knockdown of
209 certain ISGs (i.e. OAS1) enhanced cell-associated SARS-CoV-2 RNA levels modestly, these
210 effects were relatively modest compared to STING KD/KO and siRNA-specific for both cell models
211 (**Fig. 4g, h**). Collectively, these results suggest that the basally active cGAS-STING and
212 downstream type I/III IFN signaling pathways underlie the resistance to SARS-CoV-2 infection in
213 several ACE2(high) cell line models through the actions of one or more ISGs. While ablation of
214 this pathway enhances SARS-CoV-2 replication early, induction of the type I/III IFN responses at

215 later time points post-infection limits spreading infection.

216 ***cGAS-STING pathway activity underlies the basally high ISG levels in the ACE2(high) cell***
217 ***models***

218 To directly link the tonic cGAS-STING pathway activity with high basal levels of ISG expression
219 in the ACE2(high) cell models, we first interrogated the gene expression profile of WT and STING
220 KO SCC25, H596, OE21 and Detroit 562 cells by RNA-seq. Of the total of 1740 differentially
221 expressed genes in WT vs. KO conditions in a given cell line (**Supplementary data 1**), genes
222 involved in the IFN response pathways stood out as the most significantly downregulated in
223 STING KO cell lines (**Fig. S5a, S5b, Supplementary data 1**). In total, 71 genes involved in IFN
224 and inflammatory response pathways were significantly downregulated in one or more cell lines
225 upon STING KO (**Fig. 5a, Supplementary data 1**). RT-qPCR analysis of select ISGs in cGAS
226 and STING KO SCC25 cells confirmed these findings (**Fig. S5c**). In agreement with this genetic
227 evidence, pharmacological inhibition of STING by H-151, which blocks the activation-induced
228 palmitoylation and clustering of STING [52], and SN-011, which binds to the cyclic dinucleotide
229 (CDN)-binding pocket of STING and locks it in an open inactive conformation [53], reduced ISG
230 expression in a dose-dependent manner in ACE2(high) cell lines, with SCC25 and OE21 cells
231 being the most responsive to treatment (**Fig. 5b-g, S5d-g**). Pre-treatment of SCC25 cells with
232 SN-011 was sufficient to enhance SARS-CoV-2 replication, whereas H-151 had more modest
233 effects likely due to less efficient downregulation of ISG expression (**Fig. 5h, 5i**). Expectedly,
234 STING inhibition in SCC25-STING KO cells didn't further enhance SARS-CoV-2 replication (**Fig.**
235 **5h, 5i**). On the other hand, neither SN-011 nor H-151 enhanced SARS-CoV-2 replication in OE21
236 cells (**Fig. 5h, 5i**), likely due to insufficient inhibition of ISG expression by pre-treatment alone.
237 Taken together, both genetic and pharmacological evidence presented herein supports the finding
238 that tonic activation of the cGAS-STING pathway underlies the basally high ISG expression in
239 multiple airway-derived cell models.

240 ***Culture supernatants from and co-culturing with ACE2(high) cell lines induce innate***
241 ***immune activation***

242 Despite the genetic and pharmacological evidence which strongly suggested the involvement of
243 type I/III IFN pathway in mediating resistance of the ACE2(high) cells to SARS-CoV-2 replication,
244 we were unable to detect IFN-β and IFN-λ in culture supernatants. This is possibly due to low
245 level of cGAS-STING pathway activation (as also evident in P-STING and P-IRF3 blots in **Fig.**
246 **S4b**) and/or possibly unstable nature of secreted IFNs in culture media. To further evaluate the
247 resistance phenotype, we next tested whether culture supernatants from the ACE2(high) cells
248 can activate the IFN pathway in THP-1 human monocytic cells that are highly responsive to type
249 I/III IFNs. Although culture supernatants from SCC25, H596 and OE21 cells trended to trigger
250 ISG expression, as exemplified by the increase in *MX1*, the magnitude of this response was
251 comparably small to that induced by IFN-α treatment but notably higher than the STING KO
252 variants (**Fig. 6a**). Notably, co-culturing of suspension THP-1 cells with SCC25, H596 and OE21
253 cells but not their STING KO derivatives more potently induced *MX1* expression (**Fig. 6b**). A
254 similar degree of induction was observed in THP-1-cGAS KO cells (**Fig. S6a**), suggesting the
255 independence of IFN pathway activation on possible PAMPs present in SCC25, H596 and OE21
256 cells/culture medium.

257 To evaluate the levels of 2'3'-cGAMP in ACE2(high) cells, we next determined whether post-
258 nuclear fractions from our cell line panel can trigger IFN-β expression in target cells. While, 2'3'-
259 cGAMP, but not 2'2'-cGAMP, induced IFN-β expression over 10-fold in THP-1 and THP-1 cGAS
260 KO cells, PNS from the ACE2(high) cells didn't (**Fig. 6c, S6b**). Predictably, 2'3'-cGAMP didn't
261 induce IFN-β expression in the THP-1 STING KO cells (**Fig. 6d**). Overall, these experiments
262 demonstrated that the SCC25, H596 and OE21 cells likely maintain low levels of cGAS-STING-
263 dependent innate immune activation marked with phenotypically detectable levels of type I/III IFN

264 secretion.

265 ***SARS-CoV-2 antagonizes the IFN but not inflammatory pathway activity in infected cells***

266 The limited virus spread in STING KO SCC25 cells (**Fig. 4d, 4e, S4e**) prompted us to further
267 investigate the interplay between cGAS-STING-mediated activation of the IFN pathway and
268 SARS-CoV-2 infection. Despite the noted reduction in ISG expression (**Fig. 5a, S5c, S7a**), cGAS
269 and STING KO cells still mounted substantial increases in ISGs expression in response to SARS-
270 CoV-2 replication (**Fig. 7a**), nearing levels observed in WT SCC25 cells (**Fig. 7b**). In agreement
271 with prior studies [31-37], this response was mediated by sensing of SARS-CoV-2 replication
272 intermediates by RIG-I-like receptors, RIG-I and MDA5, whose knockdown abolished ISG
273 induction (**Fig. S7b**). Most notably and in agreement with prior work [54], in SARS-CoV-2-infected
274 SCC25-STING KO cells, ISG induction, as exemplified by IFIT3, was largely limited to uninfected
275 bystander cells; cells infected with SARS-CoV-2 were devoid of IFIT3 (**Fig. 7c, S7c, S7d**). Further
276 characterization of single-cell sorted infected and bystander cells revealed a general suppression
277 of ISG expression but elevated expression of numerous inflammatory mediators, including
278 *CXCL1*, *CXCL2*, *CXCL10* and *CCL20* in infected cells (**Fig. 7d, e**). These findings collectively
279 suggest that SARS-CoV-2 can efficiently antagonize IFN signaling but not IFN production or
280 inflammatory pathways in infected cells and that IFN signaling in bystander cells limits viral spread
281 in settings where ACE2 is expressed at endogenous levels.

282 ***Dissection of mechanisms that maintain tonic cGAS-STING pathway activity***

283 To identify the mechanisms that may underlie tonic activation of the cGAS-STING pathway, we
284 primarily focused on the role of TREX1 endonuclease [55,56], possible mutations within components
285 of the cGAS and STING pathway, mitochondrial DNA leakage [57,58] and the levels and activities of
286 endogenous retroviruses and transposable elements [20]. SCC25, H596, OE21 and Detroit 562
287 cells expressed equivalent levels of TREX1 (**Fig. S8A**) and while TREX1 KO modestly elevated

288 ISG expression in SCC25, H596 and Detroit 562 cells, OE21 TREX1 KO cells displayed
289 surprisingly lower levels of ISGs (**Fig. 8A, S8B**). Interrogation of the RNA-seq data (**Fig. 5A**)
290 revealed that all four cell lines expressed the common H232R variant of STING (**Fig. 8B**), which
291 more potently activates innate immunity than the less common H232 variant [59,60]. In addition,
292 H596 and Detroit 562 cells expressed the cGAS T35N and T35N/P261H variants, respectively.
293 Of note, cGAS P261H variant has recently been reported to maintain baseline innate immune
294 activation [61]. Although these naturally occurring variants can contribute to the basal levels of ISGs,
295 we did not identify canonical STING activating mutations such R284M/G or V155M more
296 commonly associated with inflammatory conditions [62]. No other mutations were identified in
297 TREX1 or ENPP1, the main 2'3'-cGAMP hydrolase. While we did not detect higher levels of
298 cytosolic mtDNA in the ACE2(high) cell lines (**Fig. S8C**), VBIT-4, a VDAC inhibitor that prevents
299 its oligomerization and subsequent mtDNA leakage into the cytosol, diminished ISG expression
300 in SCC25, OE21 and more modestly in Detroit 562 cells, but had no effect on ISG levels in H596
301 cells (**Fig. 8C**). Furthermore, extended culturing of ACE2(high) cells in the presence of nucleoside
302 analog azidothymidine (AZT), which has been shown to be active against endogenous virus
303 reverse transcriptases [63] did not reduce ISG levels (**Fig. 8D, S8D**). In agreement, we did not find
304 an association between cytosolic ERV/LINE DNA (**Fig. 8E**) or RNA levels (**Fig. S8E**) and basally
305 high ISG expression in the cell line panel. Taken together, these findings suggest that mtDNA
306 leakage combined with naturally occurring cGAS and STING variants may explain the tonic
307 cGAS-STING pathway activity in the ACE2(high) cell lines.

308 ***In primary airway cultures, SARS-CoV-2 induces ISG expression in bystander and***
309 ***antagonizes STING expression in infected cells***

310 To extend the findings from our cell line studies to a physiologically relevant model, we next
311 investigated the expression levels of two representative ISGs (i.e. IFIT2, ISG15) and STING in
312 primary human airway epithelial cells (hTECs) grown at the air-liquid interface. Of the five donors

analyzed, all except for Donor 2 appeared to express IFIT2 in a subset of cells in the absence of infection (**Fig. 9A**). SARS-CoV-2 infection resulted in an increase in IFIT2 expression in all donors (**Fig.9A**). Remarkably, as in SCC25 STING KO cells, we found that IFIT2 expression was largely limited to uninfected bystander cells (**Fig.9A-C**) and similar results were observed with ISG15 (**Fig. 9D, 9E, S9A**). All five hTECs donors endogenously expressed STING (**Fig. S9B**) and SARS-CoV-2 infection resulted in a modest increase in STING expression (**Fig. 9F, S9C**); however, we found that infected cells were largely devoid of STING (**Fig. 9F, 9G, S9C, S9D**). Inhibition of STING by both SN-011 and H-151 modestly enhanced infectious virion release (**Fig. 9H**), which in the case of H-151 correlated with a decrease in ISG expression in infected hTECs (**Fig. 9I**). In contrast, SN-011 only modestly reduced ISG expression in one Donor and ISG15 expression in all donors (**Fig. S9E**). Analysis of publicly accessible single-cell data sets revealed STING and ISG expression in healthy alveolar type-1 (AT1) human airway cells but not in alveolar type-2 (AT2) cells (**Fig. 10**), which are the primary targets of SARS-CoV-2 [64]. Together, these findings establish an inhibitory role for STING in SARS-CoV-2 replication and highlight it as a possible factor that contributes to defining the cellular tropism of SARS-CoV-2. These experiments also validate our findings from the cell line models in physiologically relevant settings and demonstrate efficient antagonism of the IFN pathway in productively infected cells.

DISCUSSION

Because ectopic expression of ACE2 allows efficient SARS-CoV-2 replication in numerous cell lines and animal models [4-7,12], it is generally thought that ACE2 is the main factor that defines the cellular tropism of SARS-CoV-2. Our findings challenge this notion and demonstrate that in cells that express endogenous levels of ACE2, baseline activation of the type I/III IFN pathway efficiently limits virus replication at a post-entry step. Interestingly, we found that ectopic expression of ACE2 overcomes the ISG-mediated restriction to SARS-CoV-2 replication in these cell models, suggesting the ability of SARS-CoV-2 to antagonize these blocks at higher

338 multiplicities of infection and possibly their saturable nature. In addition to providing novel insight
339 to molecular mechanisms that govern the cellular tropism of SARS-CoV-2, the ACE2(high) cells
340 studied here can serve as unique models to study the molecular details of innate host responses
341 against SARS-CoV-2.

342 Our study revealed that the basal activity of cGAS and STING—which have well described roles
343 in sensing of cytosolic DNA including virus replication intermediates [65,66]—underpins the IFN
344 pathway activation in three separate ACE2(high) cell lines. With regards to what activates the
345 cGAS-STING pathway, we found the involvement of mtDNA leakage in SCC25 and OE21 cells
346 and possibly naturally occurring cGAS and STING mutations that are more prone to activation in
347 the other ACE2(high) cell models. It is, however, important to emphasize that the degree of cGAS-
348 STING pathway activation in the cell lines we studied is likely low and/or present only in a
349 subpopulation of the cells in culture. This would explain why extended treatment with VBIT-4
350 reduced ISG expression despite the lack of detectable cytosolic mtDNA and 2'3'-cGAMP, the low
351 levels of IFNs present in culture supernatants and phosphorylated STING and IRF3 in cell lysates.
352 What activates the mtDNA leakage is less clear and it is possible that genomic instability
353 commonly present in cancer cell lines [67] may also contribute.

354 Activation of the cGAS-STING pathway has been shown to contribute to SARS-CoV-2
355 immunopathology and establishment of antiviral defenses [68]. In macrophages, cGAS activation
356 from engulfed DNA of dying endothelial cells near sites of tissue damage can trigger type I IFN
357 responses leading to lung inflammation in COVID-19 patients [69]. In addition, in SARS-CoV-2-
358 infected cells both mitochondrial and nuclear DNA leakage into the cytosol can activate cGAS-
359 STING signaling [69,70]. While STING agonists in uninfected cells can block SARS-CoV-2 infection
360 via triggering type I IFNs [54,71,72], pharmacological inhibition of STING reduces severe lung
361 inflammation induced by SARS-CoV-2 and improves disease outcome in mice [68]. Our study
362 supports the published antiviral functions of cGAS-STING pathway, highlights it as a key factor in

363 mounting the antiviral defenses, and further expands its role to defining the cellular tropism of
364 SARS-CoV-2 *in vitro*. Healthy gut microbiome-induced cGAS-STING activation at a basal state *in*
365 *vivo* [19] represents a particularly relevant context for our observations. SARS-CoV-2 can efficiently
366 infect cells within gastrointestinal tract *in vitro* [73,74], but it is possible that microbiota-induced
367 activation of the cGAS-STING pathway can limit SARS-CoV-2 replication within the GI tract or its
368 tropism within particular cell subsets therein. Although STING didn't appear to be involved in host
369 defense and pathology in a mouse model [75], the use of non-native K18 promoter driving ACE2
370 overexpression in tissues, which we show can decrease sensitivity to IFN-mediated inhibition, is
371 a possible caveat.

372 Our findings are also suggestive of an antagonistic relationship between SARS-CoV-2 and STING
373 in the primary HBEC-ALI cells; a significant number of productively infected cells lack STING
374 expression (**Fig. 9f, 9g, S9c, S9d**) and STING inhibitors modestly enhanced virus replication
375 while decreasing innate immune activation (**Fig. 9h, 9i, S9e**). It will be important to determine
376 whether this reduction in STING levels in infected primary airway cells is due to direct antagonism
377 by SARS-CoV-2 proteins, such as ORF3a, ORF10 and 3CLpro have been shown to antagonize
378 the cGAS-STING pathway largely through inhibition of downstream signaling [76-78]. Alternatively,
379 SARS-CoV-2 may preferentially infect of cells that lack STING and hence those cells with lower
380 levels of basal innate immune activation. We note that the effects of STING inhibitors on SARS-
381 CoV-2 replication in in primary cells was relatively modest and that only H-151 reduced innate
382 immune activation whereas SN-011 was ineffective (**Fig. 9h, 9i, S9e**). These discrepancies may
383 in part be due to the inability to fully target STING in the ciliated cells at the air-facing side; STING
384 inhibitors needed to be provided in the liquid phase to maintain ALI integrity with the assumption
385 that they would diffuse to the ciliated cells efficiently and equally. More targeted genetic ablation
386 of STING in primary cells and in vivo models will be needed to address this possible shortcoming.

387 While our data strongly suggests that cGAS-STING pathway activation underlies the resistance

388 phenotype of multiple ACE2(high) cell models, there were notable differences between these cell
389 lines as well. First, Detroit 562 cells supported only low levels of virus replication upon STING KO
390 which persisted even after ACE2 overexpression, suggesting the presence of other independent
391 blocks to replication. Second, despite successful virus binding/entry (**Fig. 1d, e**) and the notable
392 reduction in numerous IFN pathway genes upon STING and STAT1 KO (**Fig. S3k, 5a**), H596
393 cells did not support SARS-CoV-2 replication and required ectopic ACE2 expression. Given the
394 importance of TMPRSS2 in defining the cellular tropism of SARS-CoV-2 [13], it is important to note
395 that both Detroit 562 and H596 cells expressed comparably higher levels of TMPRSS2 (**Fig. S1a**),
396 suggesting the likelihood of a different post-entry block to replication. Third, pretreatment of
397 SCC25 but not OE21 cells with STING inhibitors was sufficient to enhance SARS-CoV-2
398 replication, suggesting a higher degree of STING activation in the latter, as also supported by the
399 higher levels of P-IRF3 detected in cell lysates (**Fig. S4b**). Fourth, all cell lines expressed distinct
400 sets of ISGs and inflammatory genes basally, suggesting that the SARS-CoV-2 resistance may
401 be mediated by different effector molecules. Moving forward, understanding the molecular basis
402 of these post-entry blocks through comparative analysis of the cell models presented herein can
403 reveal novel cell intrinsic mechanisms that limit SARS-CoV-2 replication.

404 IFN signaling leads to the transcriptional upregulation of hundreds of ISGs, many of which are
405 effector molecules that limit virus replication by distinct mechanisms [79,80]. Several studies have
406 reported on ISG screens and individual antiviral properties of ISGs against SARS-CoV-2, as
407 summarized recently [2]. Our findings suggest that the ISGs with previously demonstrated antiviral
408 activity against SARS-CoV-2 are unlikely to explain the resistance phenotype of the ACE2(high)
409 cells (**Fig. 4g, 4h**). Whether a dominant ISG or multiple ISGs limit SARS-CoV-2 replication in our
410 cell models remains unknown. Of note, many of the prior ISG screens have been conducted in
411 ACE2 overexpressing cells or cell lines of non-airway origin. In light of our finding that ACE2
412 overexpression relieves ISG-mediated restriction of SARS-CoV-2 replication (**Fig. 4f, S4f**), we

413 propose that the cell models studied herein provide a unique platform to discover the antiviral
414 activities of ISGs.

415 SARS-CoV-2 encodes numerous non-structural and accessory proteins that can antagonize IFN-
416 mediated innate immune responses by blocking the production of IFN-β, directly interacting with
417 IFN pathway components and inhibiting IFN signaling, or inhibiting the activities of specific ISGs
418 [81,82]. Given that ISG expression is limited to uninfected bystander cells in both SCC25 STING KO
419 cells and primary airway cultures, our findings suggest that SARS-CoV-2 replication prevents IFN
420 signaling but not IFN production in infected cells. While these findings are in agreement with a
421 SARS-CoV-2-infected gut organoid system [83], others have reported ISG expression in both
422 infected and bystander cells in a similar HBEC-ALI setting [84]. It remains to be determined whether
423 one or more of the abovementioned SARS-CoV-2 proteins is sufficient to block IFN signaling in
424 the cell models presented here.

425 Understanding the fundamental biology of how SARS-CoV-2 interacts with the innate immune
426 responses in tractable cell culture-based systems is critical to our understanding of the complex
427 SARS-CoV-2 pathogenesis *in vivo.* Our study highlights that basal activation of the cGAS-STING
428 and IFN pathways can contribute to defining the SARS-CoV-2 cellular tropism at physiologically
429 relevant ACE2 expression levels. While correlative, it is noteworthy that three of the four
430 ACE2(high)/ISG(high) cell lines (SCC25, OE21, Detroit 562) are derived from the upper airways,
431 whereby cGAS-STING mediated restriction may be operative. Our findings also demonstrate the
432 ability of SARS-CoV-2 to efficiently antagonize the IFN pathway, but not RLR-dependent innate
433 immune sensing and IFN production once productive infection is established. Further dissection
434 of these pathways may lead to the identification of actionable host cell targets that are central to
435 the complex SARS-CoV-2 pathogenesis.

436 **METHODS**

437 Our research complies with all relevant ethical regulations and all relevant protocols have been
438 approved by Washington University School of Medicine Institutional Biological and Chemical
439 Safety Committee. The human airway epithelial cells are isolated from non-living individuals, and
440 therefore research involving the use of these cells is exempt from human subjects regulations as
441 determined by the Washington University Institutional Review Board.

442 ***Cell Culture and Compounds***

443 All cell lines were maintained in a humidified incubator at 37°C with 5% CO_2 unless otherwise
444 indicated. Cell line identities were validated by short tandem repeat analysis (LabCorp, Genetica
445 Cell Line Testing) and cultures were regularly tested for mycoplasma contamination using the
446 MycoAlert mycoplasma detection kit (Lonza). HEK293T and Calu-3 (ATCC-HTB-55) cells were
447 cultured in Dulbecco's Modified Eagle's Medium (DMEM, Sigma), supplemented with 10% FBS
448 (VWR). Vero CCL-81, Vero E6 and Vero E6-TMPRSS2 (kind gift of Whelan lab [85]) cells were
449 cultured in DMEM, supplemented with 10% FBS and 10 mM HEPES buffer. The A427 lung
450 carcinoma (kind gift from Bernard Weissman Lab (UNC)) and Detroit 562 pharyngeal carcinoma
451 (ATCC-CCL-138) cell lines were cultured in Eagle's Minimum Essential Medium (EMEM,
452 Corning), supplemented with 10% FBS (Sigma), and 2 mmol/L L-glutamine (Gibco). The SCC25
453 squamous cell carcinoma (kind gift from the John Hayes Lab (UTHSC)) cell line isolated from
454 tongue was cultured in DMEM:F12 (Corning) supplemented with 10% FBS (Sigma). The H522
455 non-small cell lung adenocarcinoma (ATCC-CRL-5810), H596 adenosquamous lung carcinoma
456 (ATCC HTB-178), H1299 non-small cell lung carcinoma (ATCC CRL-5803), HCC827 lung
457 adenocarcinoma (ATCC CRL-2868), PC-9 lung adenocarcinoma (Sigma #90071810), KYSE30
458 oesophageal squamous cell carcinoma (kind gift from the John Hayes Lab), and OE21
459 oesophageal squamous cell carcinoma (Sigma # 96062201) cell lines were cultured in Roswell
460 Park Memorial Institute (RPMI) 1640 (Corning) with L-glutamine supplemented with 10% FBS

461 (Sigma). THP-1 cells (ATCC#TIB-202) and its derivatives described previously[86] were grown in
462 RPMI-1640 media supplemented with 10% heat-inactivated fetal bovine serum.

463 Primary human bronchial epithelial cells (HBECs) grown at air-liquid interface (ALI) were
464 processed as follows. Human airway epithelial cells were isolated from surgical excess of
465 tracheobronchial segments of lungs donated for transplantation as previously described and were
466 exempt from regulation by US Department of Health and Human Services regulation 45 Code of
467 Federal Regulations Part 46 [87]. Tracheobronchial cells were expanded in culture, seeded on
468 supported membranes (Transwell; Corning, Inc.), and differentiated using ALI conditions as
469 detailed before using 24-well inserts [88,89].

470 The following compounds were reconstituted in solvents following manufacturer's instructions and
471 stored in aliquots in -80. 2'3'-cGAMP (Invivogen, Cat no: tlrl-nacga23-1), 2'2'-cGAMP (Cayman,
472 Cat no: 22419, H-151 (MedChemExpress, Cat no: HY-112693, Lot no:261833), SN-011
473 (MedChemExpress, Cat no: HY-145010, Lot no: 149227), VBIT-4, azidothymidine (AZT, NIH
474 AIDS Reagents, Cat no: HRP-3485). Cells were treated as indicated in figure legends and mock-
475 treated cells were included as controls in all experiments.

476 ***Viral Strains***

477 SARS-CoV-2 strain 2019-nCoV/USA-WA1/2020 was obtained from Centers for Disease Control
478 and Prevention (a gift of Natalie Thornburg). The mNeonGreen (mNG) SARS-CoV-2 reporter
479 virus [90] was a gift of Pei-Yong Shi lab, and SARS-CoV-2 Lambda, Iota, Mu, Beta, Epsilon, Delta,
480 Kappa, and Omicron variant isolates were obtained from Dr. Michael S. Diamond. SARS-CoV-2,
481 SARS-CoV-2-mNG and variant isolates were propagated in Vero E6-TMPRSS2 at an MOI of 0.01
482 grown in DMEM (Sigma), supplemented with 2% Fetal Bovine Serum (FBS, VWR) and 10 mM
483 HEPES buffer (Corning). SARS-CoV-2 Omicron variant strain was grown in DMEM supplemented
484 with 1% FBS. After amplification, the viral stocks were titered on Vero-TMPRSS2 cells by plaque

485 assays and sequence confirmed. All experiments involving SARS-CoV-2 were performed in a
486 biosafety level 3 laboratory.

487 ***SARS-CoV-2 infections and focus-forming assay***

488 Cells seeded at 70-80% density were inoculated with virus diluted in cell culture media
489 supplemented with 2% FBS and intermittent rocking for 1 h. Virus inoculum was removed, cells
490 washed with 1x phosphate-buffered saline (PBS) and plated in cell culture media containing 10%
491 FBS. Infections were monitored by focus-forming assay, and RT-qPCR of cell-associated vRNA
492 (N sub-genomic RNA). Briefly, for focus-forming assay, Vero E6-TMPRSS2 cells were inoculated
493 with 10-fold serial dilutions of virus containing supernatants from the panel of airway cell lines,
494 incubated for 1 h at 37°C with intermittent rocking, followed by addition of 2% methylcellulose and
495 2X MEM containing 4% FBS. 30 hours post-infection cells were fixed by 4% paraformaldehyde
496 (PFA) and stained as previously described [85]. Briefly, cells were incubated with CR3022 anti-S
497 antibody (1 ug/mL)[91] overnight followed by anti-human IgG-HRP-conjugated goat secondary
498 antibody (Sigma, 1:500) for 2 h, then foci were visualized with TrueBlue peroxidase substrate
499 (KPL, #5510-0050) and manually counted under the microscope.

500 Prior to infection, HBECs were washed two times with 1× PBS to remove the mucous layer that
501 otherwise can slow down infection. HBECs were inoculated with SARS-CoV-2-mNG in DMEM-
502 supplemented with 2% FBS for two hours in a humidified incubator at 37°C, after which the initial
503 inoculum was removed, cells washed with 1xPBS and maintained at ALI for the duration of the
504 assays. Subsequently, cells were fixed with 4% paraformaldehyde and subjected to
505 immunofluorescence microscopy as detailed below.

506 ***ACE2 overexpression, lentivirus production and transduction***

507 Cell lines stably expressing human ACE2 were generated by lentiviral transduction as described
508 before[31]. Briefly, lentiviruses were produced in HEK293T cells by polyethyleneimine
509 (Polysciences)-mediated transfection using an pLV-EF1a-IRES-Puro (Addgene Plasmid
510 #85132)-based vector expressing human ACE2, psPAX2 as packaging plasmid (Addgene
511 #12260) and VSV-G expressing envelope plasmid (Addgene #12259). Cell culture supernatants
512 containing lentiviruses were collected and used to transduce SCC25, OE21, Detroit 562, H522
513 and H596 airway cell lines. Two days post transduction, cells were selected for two weeks in 2
514 μg/mL puromycin to generate bulk populations expressing ACE2.

515 ***CRISPR knockout cell lines***

516 ACE2 knockout cell lines were generated as previously stated [31]. In short, lentiviruses were
517 generated in HEK293T cells by transfection of pLentiCRISPRv2 -Puro plasmid containing a single
518 guide RNA (sgRNA) (GTACTGTAGATGGTGCTCAT) (GenScript) targeting ACE2, psPAX2
519 packaging plasmids (Addgene #12260), and pMD2.G plasmid expressing VSV-G (Addgene
520 #12259) in a ratio of 1:1:0.2 respectively using polyethyleneimine. After transduction of PC-9,
521 KYSE30, HCC827, H1299, SCC25, OE21, A427, Detroit 562, and H596 airway cell lines with the
522 resulting lentiviruses, cells were selected in 2 μg /mL puromycin for two weeks.

523 cGAS-STING pathway (i.e. cGAS, STING, TBK1, and IRF3), STAT1, and TREX1 knockout cell
524 lines were generated similarly by transduction using lentiviral particles generated using
525 pLentiCRISPRv2 -Puro encoding two separate gene-specific sgRNA per target (Table S1),
526 psPAX2, and VSV-G as described above. Following transduction, SCC25, H596, OE21, and
527 Detroit 562 cell lines were selected in 2 μg/mL puromycin for at least two weeks. In all
528 experiments, bulk populations were used for downstream analyses. cGAS and STING KO THP-
529 1 cells were explained before[86].

530 ***RNA extraction and RT-qPCR***

531 Cell associated RNA was extracted by Trizol following manufacturer's instructions (Thermo-Fisher
532 Scientific) and was subjected to RT-qPCR analysis for viral (*N* sgRNA) or cellular RNAs. SARS-
533 CoV-2 viral RNA was detected by reverse transcription and amplification using the TaqMan RNA-
534 to-CT 1-Step Kit (Thermo Fisher Scientific), utilizing the primers and probe sequences for viral
535 RNAs are as described before [76]. Briefly, reverse transcription was performed at 48 °C for
536 15 minutes, followed by a 2-minute incubation at 95 °C. Amplification was carried out over 50
537 cycles, with each cycle consisting of a 15 second denaturation step at 95 °C, followed by a 1-
538 minute annealing/extension step at 60 °C. The quantification of SARS-CoV-2 N gene RNA copies
539 was determined using a previously published internal RNA standard [92]. To study the type I/III IFN
540 response at baseline and in response to various stimuli, cellular RNA was reverse transcribed
541 with High-Capacity cDNA Reverse Transcription kit (Thermo Fisher Scientific) followed by RT-
542 qPCR analysis using PowerUp SYBR Green Master Mix (Applied Biosystems), utilizing specific
543 primers that are listed in the Table S2. RNA levels were quantified using the $2^{-\Delta\Delta CT}$ method and
544 normalized relative to *18S rRNA* as the reference target.

545 ***Viral RNA detection by RNAscope***

546 SARS-CoV-2 RNA was detected as described before (41) with minor modifications using the
547 RNAscope Multiplex Fluorescent Reagent Kit v2 (Advanced Cell Diagnostics catalog #323100).
548 One day after attachment on coverslips placed in 24-well plates, cells were infected with SARS-
549 CoV-2 at an MOI of 2 for 1 h, then washed twice with 1x PBS and fresh media was added. Cells
550 were fixed with 4% PFA at 2 hours post infection, dehydrated and stored at -20°C. On the day of
551 detection, cells were rehydrated and incubated in 0.1% Tween in PBS for 10 min and immobilized
552 on slides. Before probing, cells were first treated with hydrogen peroxide (Advanced Cell
553 Diagnostics catalog #322381) and 1:5 diluted protease III (Advanced Cell Diagnostics catalog
554 #322381) each for 10 minutes at room temperature. Immediately after, an anti-sense RNAscope
555 Probe-V-nCoV2019-S (Advanced Cell Diagnostics catalog #848561) targeting SARS-CoV-2

556 positive strand S RNA was allowed to hybridize at 40°C for 2 hr. All consecutive incubations were
557 performed at 40°C unless otherwise indicated. After probe hybridization, Amplifiers (Amp) were
558 added sequentially as follows; Amp 1 for 30 min, followed by Amp 2 for 30 min, and Amp 3 for 15
559 min. Samples were then incubated with detection reagents including horseradish peroxidase
560 (HRP)-C1 for 15 min, diluted Tyramide Signal Amplification (TSA) Vivid Fluorophore 520 (1:1500,
561 Advanced Cell Diagnostics catalog #323271) in TSA buffer (Advanced Cell Diagnostics catalog
562 #322809) for 30 min and HRP blocker for 30 min. Nuclei were stained with DAPI at room
563 temperature for 30 sec. Coverslips were mounted on slides using Prolong Gold Antifade. Images
564 were taken using a Zeiss LSM 880 Airyscan confocal microscope equipped with a 63/1.4 oil-
565 immersion objective.

566 ***Immunofluorescence microscopy***

567 SARS-CoV-2 N protein was visualized in infected cells as before [31]. Briefly, cells grown on
568 coverslips (Neuvitro, #GG-12-1.5-Collagen) were infected with SARS-CoV-2 and fixed with 4%
569 paraformaldehyde. Coverslips were washed with 1X PBS, incubated in 1% bovine serum albumin
570 (BSA) and 10% FBS in PBS containing 0.1% Tween-20 (PBST) at room temperature for 1 h.
571 Samples were then incubated in a primary mouse SARS-CoV-2 nucleocapsid (N) antibody (Sino
572 Biological Inc., Cat # 40588-T62, 1:1000) at 4 °C overnight. After washing with PBST, samples
573 were incubated in a goat anti-mouse secondary antibody conjugated to Alexa Fluor Plus 488
574 (Invitrogen, Cat# A-11029, 1:1000) at room temperature for 1 h. IFIT3, IFIT2, ISG15 and STING
575 were detected by incubation with a primary rabbit polyclonal IFIT3 antibody (Novus Biologicals
576 NBP2-32500, 1:500), rabbit polyclonal IFIT2 antibody (Novus Biologicals NBP2-15180SS, 1:500),
577 rabbit polyclonal ISG15 antibody (Proteintech 15981-1-AP, 1:250) and rabbit polyclonal STING
578 antibody (Proteintech 19851-1-AP, 1:200) respectively as described above followed by incubation
579 with a goat anti-rabbit fluorescent secondary antibody (Invitrogen Goat anti-Rabbit Alexa Fluor
580 Plus 568™, Cat# A-11036, 1:1000 or Invitrogen Goat anti-Rabbit Alexa Fluor™ Plus 647, Catalog

581 # A32733TR, 1:1000). Nuclei were stained with DAPI diluted in PBS at room temperature for
582 5 min. Finally, coverslips were washed in PBST followed by PBS and then mounted on slides
583 using Prolong Gold Antifade.

584 For confocal microscopy, samples were analyzed with a Zeiss LSM880 laser
585 scanning confocal microscope (Carl Zeiss Inc. Thornwood, NY). The system is equipped with
586 405nm diode, 488nm Argon, 543nm HeNe, and 633nm HeNe lasers. Plan-Apochromat 20X
587 numerical aperture (NA) 0.8), Plan-Apochromat 40X (NA 1.4) DIC oil, and Plan-Apochromat 63X
588 (NA 1.4) DIC oil objectives were used. ZEN black software (version 2.1 SP3) was used for
589 multichannel image acquisition and for obtaining Z stacks with optimal interval and section
590 thickness. The image analysis software Volocity with Visualization module (version 6.3)
591 (PerkinElmer, Waltham, MA) was used for 3-dimensional rendering of Z slices acquired through
592 the depth of the cell monolayers. Colocalization analysis of Z stacks was performed using the
593 Colocalization module of Volocity. For epifluorescence microscopy, images were taken using
594 Leica using either the ×4 or ×20 objective.

595 ***Immunoblotting***

596 Human cell lines were grown to 70% confluence and lysed in 1X RIPA buffer (50mM Tris-HCl pH
597 7.4, 150mM NaCl, 1mM EDTA, 0.1% SDS, 1% NP-40, 0.25% sodium deoxycholate)
598 supplemented with EDTA-free protease inhibitor cocktail (Roche). Proteins were separated by
599 SDS-PAGE on 4-12% Bis-Tris gels, transferred to a nitrocellulose membranes, blocked in
600 Intercept (PBS) blocking buffer (LI-COR) or 5% milk, and incubated with primary antibodies
601 overnight at 4°C. Washed membranes were incubated for 45 min to 1 hour at room temperature
602 in secondary antibody solution (LI-COR IRDye 680, 800; 1:10,000 in 5% milk or Intercept (PBS)
603 blocking buffer), imaged on an Odyssey® CLx scanner, and analyzed using the Image Studio
604 Software. Antibodies were used at the following dilutions: ACE2 (R&D Systems #AF933, 1:200),

605 β-actin (Sigma #A5316, 1:5000 or Santa Cruz Biotech #sc8432, 1:500), Vinculin (Santa Cruz #sc-
606 73614, 1:2000), pSTAT1-Y701 (Cell Signaling #9167, 1:1000), pSTAT1-S727 (Cell Signaling
607 #8826, 1:1000), STAT1 (Cell Signaling #14994, 1:1000), MX1 (Cell Signaling #37849, 1:1000),
608 IFIT1 (Cell Signaling #14769, 1:1000), STING (Cell Signaling #13647S, 1:1000), cGAS (Cell
609 Signaling #15102S, 1:1000), TBK1 (Cell Signaling #38066S, 1:1000), IRF3 (Cell Signaling
610 #4302S, 1:1000), SARS-CoV-2 Nucleocapsid (Sino Biological # 40588-T62, 1;1000 or # 40143-
611 MM05, 1:1000), P-STING S366 (Cell Signaling #D7C3S, 1:1000), P-IRF3 S396 (Cell Signaling
612 #4D4G, 1:1000) and TREX1 (Cell Signaling #15107S, 1:1000) antibodies.

613 ***Flow cytometry***

614 SARS-CoV-2 mNG infected cells were detached with trypsin and fixed with 4% paraformaldehyde
615 at room temperature for 20 min. After fixation, cells were collected by centrifugation, resuspended
616 in 1X PBS and subjected to flow cytometry directly or processed for staining. For staining, cells
617 were permabilized in 1X PBS supplemented with 0.5% Tween-20 (PBST) for 10 min, washed
618 once with 1X PBS and blocked by incubation in 1X PBST supplemented with 1% bovine serum
619 albumin and 10% FBS for 1h at room tempreature. Samples were then incubated in a primary
620 rabbit polyclonal antibody against IFIT3 (Novus Biologicals, NBP2-32500, 1:500) at 4 ° C
621 overnight followed by staining with a goat anti-rabbit Alexa Fluor Plus 647 (Life Technologies,
622 A32733TR, 1:1000) for 1 h at room temperature. Cells were washed in 1X PBST in between
623 antibody incubations and resuspended in 1X PBS. Flow cytometry was performed using BD LSR
624 Fortessa flow cytometer and analyzed by FlowJo software.

625 ***siRNA transfections***

626 siRNAs (Table S3) were reverse-transfected as described before [31]. In brief, 5 pmoles of siRNAs
627 for each target was complexed with 1.5 µL of Lipofectamine RNAiMAX transfection reagent in 50
628 µL of Opti-MEM following manufacturer's recommendations and added in 24-well cell culture

629 dishes. SCC25 or OE21 cells were then seeded at $1x10^5$ cells/well. At 2-days post-transfection
630 cells were infected with SARS-CoV-2 at an MOI of 2 i.u./cell, and RNA extracted 3 days later by
631 Trizol and processed for RT-qPCR analysis as above. Knockdown efficiency was assessed by
632 RT-qPCR or immunoblotting.

633 ***Analyses of IFN activity in culture supernatants and secondary messengers in the cytosol***

634 To determine whether SCC25, H596, OE21 and Detroit 562 cells actively release type I/III IFNs
635 in cell culture supernatants compared to other airway-derived cell lines, $5x10^5$ cells were plated
636 in 6-well dishes. At 24h post-plating, culture supernatants were collected, centrifuged at 500x*g* to
637 remove cell debris and 500 μl of the resultant supernatant was inoculated on $2x10^5$ THP-1 cells
638 (or its derivatives thereof, plated in 500 μl RPMI) in 24-well plates. Total RNA was isolated at 24h
639 post-inoculation by Trizol and subjected to qRT-PCR as detailed above. In a parallel set of
640 experiments, $5x10^5$ cells were plated in 6-well dishes one day prior to co-culturing. On the day of
641 co-culturing, spent cell culture medium was removed, cells washed with PBS to remove cell debris
642 and unattached cells and $1x10^6$ THP-1 cells added on top. 24h post co-culturing, THP-1 cells that
643 remain in suspension were gently removed and subjected to RNA extraction and qRT-PCR.
644 Attachment properties of airway-derived cells were visually assessed by microscopy and we
645 found no major impact in cell morphology or viability following co-culturing.

646 To assess the presence of cGAS-derived secondary messengers in airway-derived cells, THP-1
647 and THP-1 cGAS KO and THP-1 STING KO cells were inoculated with post-nuclear supernatants
648 isolated as follows. In brief, airway-derived cells grown at confluency in 10-cm culture dishes were
649 trypsinized, collected in culture media, washed with 1xPBS and resuspended in 1 ml of hypotonic
650 buffer (10 mM Tris-Cl pH 8.0, 10 mM KCl, 1 mM EDTA supplemented with complete protease
651 inhibitors (Roche)). Following 10 min incubation on ice, cells were dounce-homogenized for 40
652 strokes and lysates were centrifuged at 1000 x *g* at 4°C for 5 min. 150 μl of resultant PNS was

653 added on $2x10^5$ THP-1 cells in 24-well plates (alongside with controls including 2'3'-cGAMP and
654 2'2'-cGAMP) and IFN-β expression analyzed by qRT-PCR following RNA extraction by Trizol as
655 detailed above.

656 Cell culture supernatants were also subjected to an IFN-β ELISA assay (InvivoGen, #luex-
657 hinfbv2) or IFN-λ ELISA assay (DY1598B-05 from R&D systems) following the manufacturer's
658 instructions. The concentration of IFNs in cell culture supernatants was derived based on a
659 standard curve obtained from serial dilutions of recombinant IFNs provided by the ELISA assay.

660 ***Analysis of cytosolic mtDNA***

661 Presence of cytosolic mtDNA in the cell line panel was analyzed as described before[93]. In brief,
662 cells grown to near confluency in 10-cm dishes were collected by trypsin, washed with 1xPBS
663 and sequentially lysed in 500 μl of buffers containing digitonin, NP-40 and SDS that allow
664 permeabilization of the plasma membrane, cellular membranes including mitochondrial and
665 nuclear membrane, respectively. 50 μl of the extract was proteinase K treated and DNA extracted
666 by phenol:chloroform:isoamyl alcohol extraction. Resultant DNA was analyzed by qPCR using
667 KCNJ as the nuclear marker and MT-ND1 and MT-D-loop as mitochondrial markers. Abundance
668 of mtDNA in the cytosol was normalized relative to its total abundance in each cell type as
669 described in detail before[93].

670 ***Gene expression analysis in infected vs. bystander SCC25 cells***

671 $1x10^7$ SCC25-STING KO cells were infected with SARS-CoV-2 mNG at MOI: 1 i.u./cell for 72 hrs.
672 Cells were subsequently fixed with 4% paraformaldehyde and single-cell sorted on a BD FACS
673 Aria III platform. Infected (mNG+) and bystander (mNG-) cells were lysed in 1X Proteinase K
674 buffer (100 mM Tris-pH7.5, 50 mM NaCl, 10 mM EDTA, 1% SDS) supplemented with 20 μg of
675 Proteinase K by incubation at 55 °C for 1h by constant agitation on a thermal mixer. RNA was

676 extracted by phenol:chloroform:isoamyl alcohol and pelleted by ammonium acetate and ethanol.
677 Pelleted RNA was subjected to qRT-PCR as above.
678
679 ***RNA-seq and single-cell RNA-seq data analysis***

680 For heatmap analysis of the interferon response pathway in our cell line cohort, RNA-seq TPM
681 data for the Cancer Cell Line Encyclopedia (CCLE) was downloaded from the DepMap portal
682 (DepMap Public 18Q3). Gene sets for the interferon response pathway were extracted from
683 MsigDB's lists of HALLMARK_INTERFERON_GAMMA_RESPONSE and
684 HALLMARK_INTERFERON_ALPHA_RESPONSE genes. Hierarchical clustering and figure
685 generation was performed with the ComplexHeatmap R package. For single-cell expression
686 levels in healthy human airways, normalized counts and cell type metadata were downloaded
687 from a publicly available single-cell study [94].

688 For RNA-seq analysis of SCC25, H596, OE21, Detroit 562 cell lines and their STING CRISPR
689 derivatives, total RNA was harvested from cells grown on 6-well plates by Trizol (Life
690 Technologies) following manufacturer's instructions. 4 μg of total RNA (from n=4 replicates) was
691 subjected to Illumina stranded mRNA library generation kit and sequenced on an Illumina Nextseq
692 500 platform at 1x75. Resultant RNA-seq reads were aligned to human genome (hg19) using the
693 STAR aligner (add ref) with a mismatch rate threshold of 4% (--outFilterMismatchNoverLmax
694 0.04). "featureCounts", a read summarization program, was then used to annotate the mapped
695 reads. RNA-seq counts generated by featureCounts were processed using the edgeR package.
696 The data was filtered with "filterByExpr" with default settings, normalized, and transformed to
697 counts per million (CPM). Genes with CPM values greater than 1 were kept, and their CPM values
698 were log10 transformed. These log10-transformed CPM values were then used to perform PCA
699 using "prcomp" function in R. RNA-seq data on WT and STING knockout airway cells have been
700 deposited to the GEO Server under accession number GSE271679.

701 The “exactTest” function from edgeR was used to test for genewise differential expression
702 between WT and KO samples of each cell line using log2 CPM values, yielding logFC, P-value
703 and FDR. For the full heatmap presented in Fig. S5, both upregulated and downregulated genes
704 (|logFC| > 1) with FDR < 0.05 were considered. Z-scores of log2-transformed CPM values for all
705 selected genes were calculated and used for consensus clustering with the
706 "ConsensusClusterPlus" package. The "ComplexHeatmap" package was then used to generate
707 the heatmap.
708 For the heatmap of selected genes in Fig. 5, only those from the human gene sets
709 "HALLMARK_INFLAMMATORY_RESPONSE,"
710 "HALLMARK_INTERFERON_ALPHA_RESPONSE," and
711 "HALLMARK_INTERFERON_GAMMA_RESPONSE" retrieved from Gene Set Enrichment
712 Analysis (GSEA) were included. Differential expression results were filtered to keep only
713 downregulated genes (logFC < -1) and those with FDR < 0.05.
714 Enrichment Heatmap for gene sets: Overrepresentation analysis was performed with the enricher
715 function from the “ClusterProfiler” package, using CPM values obtained from previous steps.
716 Gene sets that were retrieved from Molecular Signatures Database (MSigDB) of GSEA were
717 selected manually and plotted using the "ComplexHeatmap" package. For enricher function, a
718 cutoff of q < 0.01 was used to define overrepresented gene sets, the minimum number of genes
719 in the set was 10 and the p-value adjustments for multiple comparisons were set to be "fdr". The
720 -log10-transformed q-values were then calculated and used for plotting the enrichment heatmap.
721 Variant Calling: VCF files were generated using BCFtools with mapped reads. SNPs (single
722 nucleotide polymorphisms) from the VCF files were filtered using the "GATK" package based on
723 the following criteria: QUAL ≥ 30.0, DP ≥ 10.0, QD ≥ 2.0, and SOR ≤ 4.0. Reads that failed to
724 meet these criteria were filtered out. SnpEff was then used to annotate the remaining SNPs.

725 ***Statistical Analysis***

726 Generally, experiments were repeated with at least two biological replicates, represented by n.
727 Each plot includes points for individual biological replicates and mean ± SEM error bars unless
728 otherwise specified. GraphPad Prism 9 software was used for statistical analysis. Statistical
729 parameters and details for each experiment are reported in respective figure legends.

730 **DATA AVAILABILITY STATEMENT**

731 RNA-seq data on WT and STING knockout airway cells have been deposited to the Gene
732 Expression Omnibus Database under accession number GSE271679 and are available at the
733 following URL: https://www.ncbi.nlm.nih.gov/geo/query/acc.cgi?acc=GSE271679. Source data
734 are provided with this paper.

735 **CODE AVAILABILITY STATEMENT**

736 Processing of the sequencing data are done by open access software and thoroughly explained
737 in the Methods section. Any additional information required to reanalyze the data reported in this
738 paper is available from the lead contact upon request.

739

740

741 **REFERENCES**

742 1 Chen, N. *et al.* Viral strategies to antagonize the host antiviral innate immunity: an
743 indispensable research direction for emerging virus-host interactions. *Emerg Microbes*
744 *Infect* **13**, 2341144 (2024). https://doi.org/10.1080/22221751.2024.2341144
745 2 Le Pen, J. & Rice, C. M. The antiviral state of the cell: lessons from SARS-CoV-2. *Curr*
746 *Opin Immunol* **87**, 102426 (2024). https://doi.org/10.1016/j.coi.2024.102426
747 3 Sievers, B. L., Cheng, M. T. K., Csiba, K., Meng, B. & Gupta, R. K. SARS-CoV-2 and
748 innate immunity: the good, the bad, and the "goldilocks". *Cell Mol Immunol* **21**, 171-183
749 (2024). https://doi.org/10.1038/s41423-023-01104-y
750 4 Walls, A. C. *et al.* Structure, Function, and Antigenicity of the SARS-CoV-2 Spike
751 Glycoprotein. *Cell* **181**, 281-292 e286 (2020). https://doi.org/10.1016/j.cell.2020.02.058
752 5 Letko, M., Marzi, A. & Munster, V. Functional assessment of cell entry and receptor
753 usage for SARS-CoV-2 and other lineage B betacoronaviruses. *Nat Microbiol* **5**, 562-569
754 (2020). https://doi.org/10.1038/s41564-020-0688-y
755 6 Hoffmann, M. *et al.* SARS-CoV-2 Cell Entry Depends on ACE2 and TMPRSS2 and Is
756 Blocked by a Clinically Proven Protease Inhibitor. *Cell* **181**, 271-280 e278 (2020).
757 https://doi.org/10.1016/j.cell.2020.02.052
758 7 Zhou, P. *et al.* A pneumonia outbreak associated with a new coronavirus of probable bat
759 origin. *Nature* **579**, 270-273 (2020). https://doi.org/10.1038/s41586-020-2012-7
760 8 Hikmet, F. *et al.* The protein expression profile of ACE2 in human tissues. *Mol Syst Biol*
761 **16**, e9610 (2020). https://doi.org/10.15252/msb.20209610
762 9 Aguiar, J. A. *et al.* Gene expression and in situ protein profiling of candidate SARS-CoV-
763 2 receptors in human airway epithelial cells and lung tissue. *Eur Respir J* **56** (2020).
764 https://doi.org/10.1183/13993003.01123-2020
765 10 Hamming, I. *et al.* Tissue distribution of ACE2 protein, the functional receptor for SARS
766 coronavirus. A first step in understanding SARS pathogenesis. *J Pathol* **203**, 631-637
767 (2004). https://doi.org/10.1002/path.1570
768 11 To, K. F. & Lo, A. W. Exploring the pathogenesis of severe acute respiratory syndrome
769 (SARS): the tissue distribution of the coronavirus (SARS-CoV) and its putative receptor,
770 angiotensin-converting enzyme 2 (ACE2). *J Pathol* **203**, 740-743 (2004).
771 https://doi.org/10.1002/path.1597
772 12 Chen, Z. *et al.* SARS-CoV-2 immunity in animal models. *Cell Mol Immunol* **21**, 119-133
773 (2024). https://doi.org/10.1038/s41423-023-01122-w
774 13 Behboudi, E. *et al.* SARS-CoV-2 mechanisms of cell tropism in various organs
775 considering host factors. *Heliyon* **10**, e26577 (2024).
776 https://doi.org/10.1016/j.heliyon.2024.e26577
777 14 Lim, S., Zhang, M. & Chang, T. L. ACE2-Independent Alternative Receptors for SARS-
778 CoV-2. *Viruses* **14** (2022). https://doi.org/10.3390/v14112535
779 15 Loske, J. *et al.* Pre-activated antiviral innate immunity in the upper airways controls early
780 SARS-CoV-2 infection in children. *Nat Biotechnol* **40**, 319-324 (2022).
781 https://doi.org/10.1038/s41587-021-01037-9
782 16 Abt, M. C. *et al.* Commensal bacteria calibrate the activation threshold of innate antiviral
783 immunity. *Immunity* **37**, 158-170 (2012). https://doi.org/10.1016/j.immuni.2012.04.011
784 17 Brown Harding, H. *et al.* Candida albicans extracellular vesicles trigger type I IFN
785 signalling via cGAS and STING. *Nat Microbiol* (2024). https://doi.org/10.1038/s41564-
786 023-01546-0
787 18 Di Domizio, J. *et al.* The commensal skin microbiota triggers type I IFN-dependent innate
788 repair responses in injured skin. *Nat Immunol* **21**, 1034-1045 (2020).
789 https://doi.org/10.1038/s41590-020-0721-6

19 Gutierrez-Merino, J., Isla, B., Combes, T., Martinez-Estrada, F. & Maluquer De Motes, C. Beneficial bacteria activate type-I interferon production via the intracellular cytosolic sensors STING and MAVS. *Gut Microbes* **11**, 771-788 (2020). https://doi.org/10.1080/19490976.2019.1707015

20 Lima-Junior, D. S. *et al.* Endogenous retroviruses promote homeostatic and inflammatory responses to the microbiota. *Cell* **184**, 3794-3811 e3719 (2021). https://doi.org/10.1016/j.cell.2021.05.020

21 Schaupp, L. *et al.* Microbiota-Induced Type I Interferons Instruct a Poised Basal State of Dendritic Cells. *Cell* **181**, 1080-1096 e1019 (2020). https://doi.org/10.1016/j.cell.2020.04.022

22 Wypych, T. P., Wickramasinghe, L. C. & Marsland, B. J. The influence of the microbiome on respiratory health. *Nat Immunol* **20**, 1279-1290 (2019). https://doi.org/10.1038/s41590-019-0451-9

23 Dickson, R. P., Erb-Downward, J. R., Martinez, F. J. & Huffnagle, G. B. The Microbiome and the Respiratory Tract. *Annu Rev Physiol* **78**, 481-504 (2016). https://doi.org/10.1146/annurev-physiol-021115-105238

24 Pattaroni, C. *et al.* Early-Life Formation of the Microbial and Immunological Environment of the Human Airways. *Cell Host Microbe* **24**, 857-865 e854 (2018). https://doi.org/10.1016/j.chom.2018.10.019

25 Lynch, S. V. & Pedersen, O. The Human Intestinal Microbiome in Health and Disease. *N Engl J Med* **375**, 2369-2379 (2016). https://doi.org/10.1056/NEJMra1600266

26 Wang, B. *et al.* Alterations in microbiota of patients with COVID-19: potential mechanisms and therapeutic interventions. *Signal Transduct Target Ther* **7**, 143 (2022). https://doi.org/10.1038/s41392-022-00986-0

27 Sulaiman, I. *et al.* Microbial signatures in the lower airways of mechanically ventilated COVID-19 patients associated with poor clinical outcome. *Nat Microbiol* **6**, 1245-1258 (2021). https://doi.org/10.1038/s41564-021-00961-5

28 Llorens-Rico, V. *et al.* Clinical practices underlie COVID-19 patient respiratory microbiome composition and its interactions with the host. *Nat Commun* **12**, 6243 (2021). https://doi.org/10.1038/s41467-021-26500-8

29 Zuo, T. *et al.* Alterations in Fecal Fungal Microbiome of Patients With COVID-19 During Time of Hospitalization until Discharge. *Gastroenterology* **159**, 1302-1310 e1305 (2020). https://doi.org/10.1053/j.gastro.2020.06.048

30 Zuo, T. *et al.* Alterations in Gut Microbiota of Patients With COVID-19 During Time of Hospitalization. *Gastroenterology* **159**, 944-955 e948 (2020). https://doi.org/10.1053/j.gastro.2020.05.048

31 Puray-Chavez, M. *et al.* Systematic analysis of SARS-CoV-2 infection of an ACE2-negative human airway cell. *Cell Rep* **36**, 109364 (2021). https://doi.org/10.1016/j.celrep.2021.109364

32 Sampaio, N. G. *et al.* The RNA sensor MDA5 detects SARS-CoV-2 infection. *Sci Rep* **11**, 13638 (2021). https://doi.org/10.1038/s41598-021-92940-3

33 Rebendenne, A. *et al.* SARS-CoV-2 triggers an MDA-5-dependent interferon response which is unable to control replication in lung epithelial cells. *J Virol* (2021). https://doi.org/10.1128/JVI.02415-20

34 Yin, X. *et al.* MDA5 Governs the Innate Immune Response to SARS-CoV-2 in Lung Epithelial Cells. *Cell Rep* **34**, 108628 (2021). https://doi.org/10.1016/j.celrep.2020.108628

35 Kouwaki, T., Nishimura, T., Wang, G. & Oshiumi, H. RIG-I-Like Receptor-Mediated Recognition of Viral Genomic RNA of Severe Acute Respiratory Syndrome Coronavirus-2 and Viral Escape From the Host Innate Immune Responses. *Front Immunol* **12**, 700926 (2021). https://doi.org/10.3389/fimmu.2021.700926

36 Thorne, L. G. *et al.* SARS-CoV-2 sensing by RIG-I and MDA5 links epithelial infection to macrophage inflammation. *EMBO J* **40**, e107826 (2021). https://doi.org/10.15252/embj.2021107826

37 Yang, D. M., Geng, T. T., Harrison, A. G. & Wang, P. H. Differential roles of RIG-I like receptors in SARS-CoV-2 infection. *Mil Med Res* **8**, 49 (2021). https://doi.org/10.1186/s40779-021-00340-5

38 Blanco-Melo, D. *et al.* Imbalanced Host Response to SARS-CoV-2 Drives Development of COVID-19. *Cell* **181**, 1036-1045 e1039 (2020). https://doi.org/10.1016/j.cell.2020.04.026

39 Lei, X. *et al.* Activation and evasion of type I interferon responses by SARS-CoV-2. *Nat Commun* **11**, 3810 (2020). https://doi.org/10.1038/s41467-020-17665-9

40 Hatton, C. F. *et al.* Delayed induction of type I and III interferons mediates nasal epithelial cell permissiveness to SARS-CoV-2. *Nat Commun* **12**, 7092 (2021). https://doi.org/10.1038/s41467-021-27318-0

41 Chu, H. *et al.* Comparative replication and immune activation profiles of SARS-CoV-2 and SARS-CoV in human lungs: an ex vivo study with implications for the pathogenesis of COVID-19. *Clin Infect Dis* (2020). https://doi.org/10.1093/cid/ciaa410

42 Stukalov, A. *et al.* Multi-level proteomics reveals host-perturbation strategies of SARS-CoV-2 and SARS-CoV. *bioRxiv*, 2020.2006.2017.156455 (2020). https://doi.org/10.1101/2020.06.17.156455

43 Hadjadj, J. *et al.* Impaired type I interferon activity and inflammatory responses in severe COVID-19 patients. *Science* **369**, 718-724 (2020). https://doi.org/10.1126/science.abc6027

44 Galani, I. E. *et al.* Untuned antiviral immunity in COVID-19 revealed by temporal type I/III interferon patterns and flu comparison. *Nat Immunol* **22**, 32-40 (2021). https://doi.org/10.1038/s41590-020-00840-x

45 Bastard, P. *et al.* Autoantibodies against type I IFNs in patients with life-threatening COVID-19. *Science* **370** (2020). https://doi.org/10.1126/science.abd4585

46 Goenka, A. *et al.* Young infants exhibit robust functional antibody responses and restrained IFN-gamma production to SARS-CoV-2. *Cell Rep Med* **2**, 100327 (2021). https://doi.org/10.1016/j.xcrm.2021.100327

47 Hoffmann, M. *et al.* Evidence for an ACE2-Independent Entry Pathway That Can Protect from Neutralization by an Antibody Used for COVID-19 Therapy. *mBio* **13**, e0036422 (2022). https://doi.org/10.1128/mbio.00364-22

48 Guo, K., Barrett, B. S., Mickens, K. L., Hasenkrug, K. J. & Santiago, M. L. Interferon Resistance of Emerging SARS-CoV-2 Variants. *bioRxiv* (2021). https://doi.org/10.1101/2021.03.20.436257

49 Danziger, O., Patel, R. S., DeGrace, E. J., Rosen, M. R. & Rosenberg, B. R. Inducible CRISPR activation screen for interferon-stimulated genes identifies OAS1 as a SARS-CoV-2 restriction factor. *PLoS Pathog* **18**, e1010464 (2022). https://doi.org/10.1371/journal.ppat.1010464

50 Martin-Sancho, L. *et al.* Functional landscape of SARS-CoV-2 cellular restriction. *Mol Cell* **81**, 2656-2668 e2658 (2021). https://doi.org/10.1016/j.molcel.2021.04.008

51 Wickenhagen, A. *et al.* A prenylated dsRNA sensor protects against severe COVID-19. *Science* **374**, eabj3624 (2021). https://doi.org/10.1126/science.abj3624

52 Haag, S. M. *et al.* Targeting STING with covalent small-molecule inhibitors. *Nature* **559**, 269-273 (2018). https://doi.org/10.1038/s41586-018-0287-8

53 Hong, Z. *et al.* STING inhibitors target the cyclic dinucleotide binding pocket. *Proc Natl Acad Sci U S A* **118** (2021). https://doi.org/10.1073/pnas.2105465118

54 Li, M. *et al.* Pharmacological activation of STING blocks SARS-CoV-2 infection. *Sci Immunol* **6** (2021). https://doi.org/10.1126/sciimmunol.abi9007

892 55 Ablasser, A. *et al.* TREX1 deficiency triggers cell-autonomous immunity in a cGAS-
893 dependent manner. *J Immunol* **192**, 5993-5997 (2014).
894 https://doi.org/10.4049/jimmunol.1400737
895 56 Stetson, D. B., Ko, J. S., Heidmann, T. & Medzhitov, R. Trex1 prevents cell-intrinsic
896 initiation of autoimmunity. *Cell* **134**, 587-598 (2008).
897 https://doi.org/10.1016/j.cell.2008.06.032
898 57 Rongvaux, A. *et al.* Apoptotic caspases prevent the induction of type I interferons by
899 mitochondrial DNA. *Cell* **159**, 1563-1577 (2014).
900 https://doi.org/10.1016/j.cell.2014.11.037
901 58 West, A. P. *et al.* Mitochondrial DNA stress primes the antiviral innate immune response.
902 *Nature* **520**, 553-557 (2015). https://doi.org/10.1038/nature14156
903 59 Froechlich, G. *et al.* The common H232 STING allele shows impaired activities in DNA
904 sensing, susceptibility to viral infection, and in monocyte cell function, while the HAQ
905 variant possesses wild-type properties. *Sci Rep* **13**, 19541 (2023).
906 https://doi.org/10.1038/s41598-023-46830-5
907 60 Kennedy, R. B. *et al.* Polymorphisms in STING Affect Human Innate Immune Responses
908 to Poxviruses. *Front Immunol* **11**, 567348 (2020).
909 https://doi.org/10.3389/fimmu.2020.567348
910 61 Kazmierski, J. *et al.* A Baseline Cellular Antiviral State Is Maintained by cGAS and Its
911 Most Frequent Naturally Occurring Variant rs610913. *J Immunol* **209**, 535-547 (2022).
912 https://doi.org/10.4049/jimmunol.2100685
913 62 Decout, A., Katz, J. D., Venkatraman, S. & Ablasser, A. The cGAS-STING pathway as a
914 therapeutic target in inflammatory diseases. *Nat Rev Immunol* **21**, 548-569 (2021).
915 https://doi.org/10.1038/s41577-021-00524-z
916 63 Contreras-Galindo, R., Dube, D., Fujinaga, K., Kaplan, M. H. & Markovitz, D. M.
917 Susceptibility of Human Endogenous Retrovirus Type K to Reverse Transcriptase
918 Inhibitors. *J Virol* **91** (2017). https://doi.org/10.1128/JVI.01309-17
919 64 Hou, Y. J. *et al.* SARS-CoV-2 Reverse Genetics Reveals a Variable Infection Gradient in
920 the Respiratory Tract. *Cell* **182**, 429-446 e414 (2020).
921 https://doi.org/10.1016/j.cell.2020.05.042
922 65 Ge, Z. & Ding, S. Regulation of cGAS/STING signaling and corresponding immune
923 escape strategies of viruses. *Front Cell Infect Microbiol* **12**, 954581 (2022).
924 https://doi.org/10.3389/fcimb.2022.954581
925 66 Hertzog, J. & Rehwinkel, J. Regulation and inhibition of the DNA sensor cGAS. *EMBO*
926 *Rep* **21**, e51345 (2020). https://doi.org/10.15252/embr.202051345
927 67 Mackenzie, K. J. *et al.* cGAS surveillance of micronuclei links genome instability to
928 innate immunity. *Nature* **548**, 461-465 (2017). https://doi.org/10.1038/nature23449
929 68 Li, H., Zhou, F. & Zhang, L. STING, a critical contributor to SARS-CoV-2
930 immunopathology. *Signal Transduct Target Ther* **7**, 106 (2022).
931 https://doi.org/10.1038/s41392-022-00967-3
932 69 Domizio, J. D. *et al.* The cGAS-STING pathway drives type I IFN immunopathology in
933 COVID-19. *Nature* **603**, 145-151 (2022). https://doi.org/10.1038/s41586-022-04421-w
934 70 Zhou, Z. *et al.* Sensing of cytoplasmic chromatin by cGAS activates innate immune
935 response in SARS-CoV-2 infection. *Signal Transduct Target Ther* **6**, 382 (2021).
936 https://doi.org/10.1038/s41392-021-00800-3
937 71 Humphries, F. *et al.* A diamidobenzimidazole STING agonist protects against SARS-
938 CoV-2 infection. *Sci Immunol* **6** (2021). https://doi.org/10.1126/sciimmunol.abi9002
939 72 Liu, W. *et al.* Activation of STING Signaling Pathway Effectively Blocks Human
940 Coronavirus Infection. *J Virol* **95** (2021). https://doi.org/10.1128/JVI.00490-21

941 73 Ding, S. & Liang, T. J. Is SARS-CoV-2 Also an Enteric Pathogen With Potential Fecal-
942 Oral Transmission? A COVID-19 Virological and Clinical Review. *Gastroenterology* **159**,
943 53-61 (2020). https://doi.org/10.1053/j.gastro.2020.04.052
944 74 Durairajan, S. S. K. *et al.* Gastrointestinal Manifestations of SARS-CoV-2: Transmission,
945 Pathogenesis, Immunomodulation, Microflora Dysbiosis, and Clinical Implications.
946 *Viruses* **15** (2023). https://doi.org/10.3390/v15061231
947 75 Marino, G. *et al.* STING is redundant for host defense and pathology of COVID-19-like
948 disease in mice. *Life Sci Alliance* **6** (2023). https://doi.org/10.26508/lsa.202301997
949 76 Han, L. *et al.* SARS-CoV-2 ORF10 antagonizes STING-dependent interferon activation
950 and autophagy. *J Med Virol* **94**, 5174-5188 (2022). https://doi.org/10.1002/jmv.27965
951 77 Su, J. *et al.* SARS-CoV-2 ORF3a inhibits cGAS-STING-mediated autophagy flux and
952 antiviral function. *J Med Virol* **95**, e28175 (2023). https://doi.org/10.1002/jmv.28175
953 78 Rui, Y. *et al.* Unique and complementary suppression of cGAS-STING and RNA
954 sensing- triggered innate immune responses by SARS-CoV-2 proteins. *Signal Transduct*
955 *Target Ther* **6**, 123 (2021). https://doi.org/10.1038/s41392-021-00515-5
956 79 Schoggins, J. W. Interferon-Stimulated Genes: What Do They All Do? *Annu Rev Virol* **6**,
957 567-584 (2019). https://doi.org/10.1146/annurev-virology-092818-015756
958 80 Lazear, H. M., Schoggins, J. W. & Diamond, M. S. Shared and Distinct Functions of
959 Type I and Type III Interferons. *Immunity* **50**, 907-923 (2019).
960 https://doi.org/10.1016/j.immuni.2019.03.025
961 81 Sa Ribero, M., Jouvenet, N., Dreux, M. & Nisole, S. Interplay between SARS-CoV-2 and
962 the type I interferon response. *PLoS Pathog* **16**, e1008737 (2020).
963 https://doi.org/10.1371/journal.ppat.1008737
964 82 Setaro, A. C. & Gaglia, M. M. All hands on deck: SARS-CoV-2 proteins that block early
965 anti-viral interferon responses. *Curr Res Virol Sci* **2**, 100015 (2021).
966 https://doi.org/10.1016/j.crviro.2021.100015
967 83 Triana, S. *et al.* Single-cell analyses reveal SARS-CoV-2 interference with intrinsic
968 immune response in the human gut. *Mol Syst Biol* **17**, e10232 (2021).
969 https://doi.org/10.15252/msb.202110232
970 84 Ravindra, N. G. *et al.* Single-cell longitudinal analysis of SARS-CoV-2 infection in human
971 airway epithelium identifies target cells, alterations in gene expression, and cell state
972 changes. *PLoS Biol* **19**, e3001143 (2021). https://doi.org/10.1371/journal.pbio.3001143
973 85 Case, J. B. *et al.* Neutralizing Antibody and Soluble ACE2 Inhibition of a Replication-
974 Competent VSV-SARS-CoV-2 and a Clinical Isolate of SARS-CoV-2. *Cell Host Microbe*
975 **28**, 475-485 e475 (2020). https://doi.org/10.1016/j.chom.2020.06.021
976 86 Eschbach, J. E. *et al.* HIV-1 capsid stability and reverse transcription are finely balanced
977 to minimize sensing of reverse transcription products via the cGAS-STING pathway.
978 *mBio* **15**, e0034824 (2024). https://doi.org/10.1128/mbio.00348-24
979 87 Horani, A. *et al.* Whole-exome capture and sequencing identifies HEATR2 mutation as a
980 cause of primary ciliary dyskinesia. *Am J Hum Genet* **91**, 685-693 (2012).
981 https://doi.org/10.1016/j.ajhg.2012.08.022
982 88 You, Y., Richer, E. J., Huang, T. & Brody, S. L. Growth and differentiation of mouse
983 tracheal epithelial cells: selection of a proliferative population. *Am J Physiol Lung Cell*
984 *Mol Physiol* **283**, L1315-1321 (2002). https://doi.org/10.1152/ajplung.00169.2002
985 89 Horani, A. *et al.* Establishment of the early cilia preassembly protein complex during
986 motile ciliogenesis. *Proc Natl Acad Sci U S A* **115**, E1221-E1228 (2018).
987 https://doi.org/10.1073/pnas.1715915115
988 90 Xie, X. *et al.* An Infectious cDNA Clone of SARS-CoV-2. *Cell Host Microbe* **27**, 841-848
989 e843 (2020). https://doi.org/10.1016/j.chom.2020.04.004

990 91 Case, J. B., Bailey, A. L., Kim, A. S., Chen, R. E. & Diamond, M. S. Growth, detection,
991 quantification, and inactivation of SARS-CoV-2. *Virology* **548**, 39-48 (2020).
992 https://doi.org/10.1016/j.virol.2020.05.015
993 92 Shema Mugisha, C., Vuong, H. R., Puray-Chavez, M. & Kutluay, S. B. A facile Q-RT-
994 PCR assay for monitoring SARS-CoV-2 growth in cell culture. *bioRxiv* (2020).
995 https://doi.org/10.1101/2020.06.26.174698
996 93 Bryant, J. D., Lei, Y., VanPortfliet, J. J., Winters, A. D. & West, A. P. Assessing
997 Mitochondrial DNA Release into the Cytosol and Subsequent Activation of Innate
998 Immune-related Pathways in Mammalian Cells. *Curr Protoc* **2**, e372 (2022).
999 https://doi.org/10.1002/cpz1.372
1000 94 Deprez, M. *et al.* A Single-Cell Atlas of the Human Healthy Airways. *Am J Respir Crit*
1001 *Care Med* **202**, 1636-1645 (2020). https://doi.org/10.1164/rccm.201911-2199OC
1002

1003 **ACKNOWLEDGEMENTS**

1004 This work was supported in part by a V Foundation grant (T2014-009) to M.B. Major, a T32
1005 training grant (T32CA009547-34) to K.M.L., a F31 grant to J.E.E. (AI167695). We thank the Miner
1006 lab for STING CRISPR plasmid and the Molecular Microbiology Imaging Facility (Wandy L.
1007 Beatty) for help with confocal microscopy and data analysis. We thank members of the Lopez,
1008 Lenschow, Diamond, Orvedahl and Boon labs for reagents and critical input. We opted to cite
1009 recent review articles where appropriate and apologize to colleagues whose work we were unable
1010 to cite due to citation limits.

1011 **AUTHOR CONTRIBUTIONS**

1012 M. P-C., K.M.L., M.B.M., D.G. and S.B.K. conceptualized the study; M. P-C., J.E.E., K.M.L., S.D.,
1013 M.B.M., D.G., S.L.B. and S.B.K. designed the methodology. M. P-C., J.E.E., M.X., K.M.L., J.P.,
1014 J.X., Z.Z.., S.M., Q.W., D.Q.L., S.D., G.H. and S.B.K performed the experiments. Q.Z., R.J. and
1015 D.G. performed statistical and bioinformatics analysis. M. P-C., M.B.M., D.G. and S.B.K. wrote
1016 the manuscript with input from all the authors.

1017 **COMPETING INTERESTS STATEMENT**

1018 The authors declare no competing interests.

1019

1020 **FIGURE LEGENDS**

1021 **Figure 1**. **SARS-CoV-2 replication is blocked at a post-entry stage in a subset of airway-**
1022 **derived cell lines that endogenously express ACE2. (a)** The indicated airway-derived cell lines
1023 were inoculated with WT SARS-CoV-2 (2019-nCoV/USA-WA1/2020) at a MOI: 0.15 i.u./cell. RT-
1024 qPCR analysis of cell-associated SARS-CoV-2 N sgRNA (copies/cell) at 4 and 72 hpi is shown.
1025 Data show the average of 2 independent experiments, errors bars denote the range. **(b)** Focus
1026 forming assay performed on culture supernatants of the indicated cells infected with SARS-CoV-
1027 2 for 72 hpi (from panel A). Data show focus forming units per mL (FFU/mL, log transformed) from
1028 two independent experiments, error bars show the SEM. **(c)** Polyclonal pools of ACE2 knockout
1029 (ACE2-KO) and control cell lines transduced with a non-targeting sgRNA (NT) were infected with
1030 WT SARS-CoV-2 at a MOI: 2 i.u./cell. RT-qPCR analysis of cell-associated viral RNA (sgRNA N)
1031 at 72 hpi is shown from two biological replicates. Data show the mean, error bars show the SEM,
1032 **p< 0.01 where significance was assessed by multiple unpaired t-tests. **(d)** Polyclonal pools of
1033 ACE2 KO and non-targeting control (NT) cell lines were infected with WT SARS-CoV-2 at a MOI:
1034 2 i.u./cell. In situ hybridization of incoming viral RNA (green) at 2 hpi was performed as detailed
1035 in Methods. Nuclear DAPI staining is shown in blue. **(e)** Quantification of data presented in Panel
1036 D. Puncta of SARS-CoV-2 RNA was counted in ~200 cells per cell line from two independent
1037 experiments. The average number of RNA puncta per condition is shown in the graph. Source
1038 data are provided as a Source Data file.

1039 **Figure 2**. **ACE2(high) airway-derived cell lines that are resistant to SARS-CoV-2 replication**
1040 **express high baseline levels of type I IFN pathway genes. (a)** Hierarchical clustering of IFN
1041 response pathway RNA expression levels downloaded from CCLE. The heatmap displays z-
1042 scored $\log_2$(TPM) values. **(b-e)** RT-qPCR analysis of representative ISGs including *IFIT1, MX1,*
1043 *IRF9* and *STAT1* in uninfected cells. Expression levels are normalized relative to Calu-3 cells (set
1044 to 1). Data show the mean from n=2 (H596 and Calu-3) or 4 (other cells) independent biological

1045 replicates, error bars denote SEM. **(f)** Immunoblot showing pSTAT1 (Y701 and S727), STAT1,
1046 IRF7, IRF9, MX1, IFIT1 and Vinculin levels across airway-derived cell lines (not infected). Blots
1047 are representative of two independent experiments. **(g, h)** Airway cell lines were infected with
1048 SARS-CoV-2 at a MOI of 2 i.u./cell and expression of *IFIT1* and *IFIT2* in was analyzed by RT-
1049 qPCR at 4 and 72 hpi. Y-axes indicate ISG fold induction at 72 hpi relative to 4hpi. Data show the
1050 mean from n=3 independent replicates, errors bars show the SEM. Source data are provided as
1051 a Source Data file.

1052 **Figure 3**. **Basally active type I IFN pathway limits SARS-CoV-2 replication in a subset of**
1053 **ACE2(high) cells. (a, b)** SCC25, H596, OE21, Detroit 562 and Calu-3 cells were pretreated with
1054 1 μM ruxolitinib for 24 hours. *IFIT1* (**a**) and *MX1* (**b**) expression was analyzed by RT-qPCR and
1055 expression levels are shown relative to untreated Calu-3 cells (set to 1). Data show the mean
1056 from n=2 (H596 and Calu-3) and 4 (other cells) independent biological replicates, error bars show
1057 the SEM. **(c)** SCC25, H596, OE21 and Detroit 562 cells were pretreated with DMSO (mock) or 1
1058 μM ruxolitinib for 24 hours and infected with SARS-CoV-2 at a MOI of 2 i.u./cell in presence of
1059 DMSO or 1 μM ruxolitinib. RT-qPCR analysis shows cell-associated viral RNA levels at 72 hpi.
1060 Data show the mean from n=4 independent replicates, error bars show the SEM. **(d-g)** Polyclonal
1061 populations of SCC25 cells knocked out (KO) for IFNAR (**d**) or STAT1 (**e**) using two independent
1062 sgRNAs or transduced with a non-targeting (NT) control and SCC25 cells transfected with 3
1063 separate siRNAs targeting STAT2 (**f**), IRF9 (**g**), or a non-targeting control (NT) were infected with
1064 SARS-CoV-2 at a MOI of 2 i.u./cell. Cell-associated viral RNA was analyzed by RT-qPCR at 72
1065 hpi. Y-axes indicate the relative expression ratio between knockdown (KD) or knockout (KO) and
1066 the respective NT samples. Data display the mean of n=5 (**d, e**) and n=6 (**f, g**) independent
1067 replicates, error bars denote the SEM. Source data are provided as a Source Data file.

1068 **Figure 4. A constitutively active cGAS-STING pathway limits SARS-CoV-2 replication in**
1069 **SCC25 cells. (a)** SCC25 cells transfected with siRNAs or a non-targeting control (NT) were
1070 infected with SARS-CoV-2 at an MOI of 2 i.u./cell for 72 h. Data show the ratio of cell-associated
1071 viral RNA between knockdown (KD) and NT samples. Data display the mean of 2 (NLRP1-3,
1072 NLRP3-1, NLRP3-2, NLRC5-1, NLRC5-2) or 4 (other targets) biological replicates, with error bars
1073 representing SEM. **(b)** SCC25 cGAS, STING, TBK1 and IRF3 KO cells or NT controls were
1074 infected with SARS-CoV-2 at MOI: 2 i.u./cell for 72h. Cell-associated viral N RNA from 5 replicates
1075 is shown, error bars show the SEM. $p < 0.0001$ significance (compared to NT-1) was assessed
1076 by a one-way ANOVA with Dunnett correction. **(c)** Immunoblots (representative of n=2) show
1077 SARS-CoV-2 N, cGAS, STING, TBK1, IRF3 and β-actin expression levels in SCC25 cells from
1078 panel B. **(d)** SCC25 STING KO cells were infected with SARS-CoV-2-mNG at a MOI:2 i.u./cell.
1079 NG-positive cells were enumerated by flow cytometry at 24, 48 and 72 hpi and represented as
1080 percentage of total population. Data show the mean of n=5 independent experiments, error bars
1081 denote the SEM. **(e)** SCC25 STING KO and NT control cells were pretreated for 24 hours and
1082 infected (MOI:2 i.u./cell) in the absence (DMSO) and presence of 1 μM ruxolitinib with SARS-
1083 CoV-2-mNG. NG-positive cells were enumerated by flow cytometry at 72 hpi and represented as
1084 percentage of total population. Data show the mean of n=4 independent experiments, error bars
1085 denote the SEM. *P* values are assessed by two-way ANOVA and Šidák multiple test correction.
1086 (**f**) Cells ectopically expressing ACE2 were infected at a MOI: 0.1 i.u./cell with SARS-CoV-2 WT.
1087 Cell-associated SARS-CoV-2 RNA at 2 and 24 hpi is shown from n=2 replicates. Data show the
1088 mean, error bars denote SEM. (**g, h**) SCC25 (**g**) and OE21 (**h**) cells were transfected with 2
1089 distinct siRNAs or a NT control, infected with SARS-CoV-2 and analyzed as in panel A. Data
1090 display the mean of n=3 biological replicates, with error bars representing SEM. Source data are
1091 provided as a Source Data file.

1092 **Figure 5. Genetic ablation and chemical inhibition of STING reduces basal ISG levels and**
1093 **enhances SARS-CoV-2 replication. (a)** WT and STING KO SCC25, H596, OE21 and Detroit
1094 562 cells were subjected to RNA-seq analysis. Heatmap shows differentially expressed genes
1095 (absolute $\log_2$ fold change of >2 and an adjusted *q* value of <0.05 from n=4 independent replicates
1096 for each cell type) in the IFN and inflammatory pathways in any given cell line between the WT
1097 vs. STING KO variant. (**b-g**) RT-qPCR analysis of *IFIT2, MX1* and *IFIT3* in uninfected SCC25,
1098 H596, OE21 and Detroit 562 cells treated with increasing concentrations of SN-011 (**b-d**) and H-
1099 151 (**e-g**) for 48 h. Data show the mean from n=2 independent biological replicates, error bars
1100 show SEM (**h-i**) WT and STING KO SCC25 and STING KO cells were pre-treated with 20 μM
1101 SN-011 (**h**) or H-151 (**i**) for 24h were infected with WT SARS-CoV-2 at MOI: 1 i.u./cell for 72h.
1102 Data show the copies of cell-associated SARS-CoV-2 N RNA in compound-treated cells
1103 normalized relative to mock-treated samples. Data show the mean from n=3 independent
1104 biological replicates, error bars show SEM. Significance was assessed by multiple unpaired two-
1105 tailed t-tests and *p* values provided in the figure. Source data are provided as a Source Data file.

1106 **Figure 6. Cell culture supernatants but not cell lysates from SCC25, H596 and OE21 cells**
1107 **trigger innate immune activation.** (**a, b**) *MX1* expression was analyzed by RT-qPCR in THP-1
1108 cells treated with cell culture supernatants from (**a**) or co-cultured with (**b**) the indicated cell line
1109 panel as explained in Methods. *MX1* expression is normalized relative to mock-treated cells. THP-
1110 1 cells treated with 1000 u/ml IFN-α serves as the positive control. Data show the mean induction
1111 from n=3 independent biological replicates, error bars display the SEM. *p* values were calculated
1112 by multiple unpaired t-tests with Welch's correction.. (**c, d**) THP-1 or THP-1 STING KO cells were
1113 treated with post-nuclear supernatants (PNS) from the indicated cells, 10 μg/ml 2'3'-cGAMP or
1114 10 μg/ml 2'2'-cGAMP for 24 h, as explained in Methods. *IFN-β* expression was analyzed by RT-
1115 qPCR and normalized relative to 2'2'-cGAMP-treated samples. Data show the mean from n=2

1116 independent experiments, error bars show the SEM. Source data are provided as a Source Data
1117 file.

1118 **Figure 7**. **SARS-CoV-2 antagonizes the IFN pathway but not IFN synthesis or inflammatory**
1119 **pathways in infected cells. (a)** Relative expression of ISGs including *ISG15, IFIT1, IFIT2, IFIT3*
1120 *and IRF7* in SCC25 cGAS KO, STING KO or NT control cells infected with SARS-CoV-2 at a MOI
1121 of 2 i.u./cell. Cells were collected at 72 hpi and ISG expression analyzed by RT-qPCR. Data show
1122 the fold induction of ISGs in infected over uninfected cells from n=3 biological replicates, errors
1123 bars show the SEM. **(b, c**) SCC25 STING KO or NT control cells were infected with SARS-CoV-
1124 2 at an MOI of 2 i.u./cell. Immunofluorescence detection for IFIT3 expression (in red) and SARS-
1125 CoV-2 nucleocapsid (N) viral protein (in green), and cellular nuclei (DAPI, in blue) at 72hpi from
1126 a representative experiment (n = 2) are shown. Images were collected with an epifluorescence
1127 microscope, 4X objective (**b**) or Zeiss LSM 880 Airyscan confocal microscope equipped with a
1128 ×63/1.4 objective (**c**) as detailed in Methods. Scale bars = 250 μm (**b**) or 10 μm (**c**). (**d, e**) SCC25
1129 STING KO cells were infected with SARS-CoV-2-mNG at MOI:1 i.u./cell and cells were single-
1130 cell sorted at 72 hpi to isolate infected (mNG positive) and bystander cells as detailed in Methods.
1131 Expression of the indicated ISGs (**d**) and inflammatory genes (**e**) were analyzed by RT-qPCR in
1132 these sorted cell populations. Data show the mean from two independent replicates, error bars
1133 show the SEM. Source data are provided as a Source Data file.

1134 **Figure 8. Analysis of mechanisms that underlie tonic cGAS-STING activation in the**
1135 **ISG(high) cell lines. (a)** Polyclonal populations of SCC25, H596, OE21 and Detroit 562 cells
1136 knocked out (KO) for TREX1 using two separate sgRNAs or wild-type (WT) controls were
1137 analyzed for *IFIT2* expression by RT-qPCR. Data show the relative expression of *IFIT2* in KO
1138 cells compared parental controls (set to 1) from n=3 (OE21) or 6 (SCC25, H596, Detroit 562)
1139 replicates, error bars show the SEM. (**b**) cGAS and STING variants present in the indicated cell
1140 lines derived from RNA-seq data. (**c, d**) SCC25, H596, OE21 and Detroit 562 cells grown in the

1141 presence of 10 μM VBIT-4 for 4 days (**c**) or 500 μM AZT for 3 days (**d**). *IFIT1*, *IFIT2* and *IRF7*
1142 expression was analyzed by RT-qPCR and normalized relative to mock-treated controls (set to
1143 1). Data show the mean from n=3 replicates, error bars show the SEM. (**e**) Following subcellular
1144 fractionation (see Methods), levels of the indicated HERV and LINE DNA elements were
1145 assessed by qPCR in the cytosol and nucleus. Data show the relative levels of each element in
1146 the cytosol relative to the nuclear extract in each cell type (n=2, error bars show SEM). Source
1147 data are provided as a Source Data file.

1148 **Figure 9. Analysis of ISG and STING expression in SARS-CoV-2-infected primary human**
1149 **airway epithelial cells (hTECs) grown at ALI. (a-e)** hTECs from five donors grown at ALI were
1150 infected with SARS-CoV-2-mNG at a MOI of 2 i.u./cell and fixed at 72 hpi. Immunofluorescence
1151 detection for IFIT2 expression (in red), ISG15, mNG (in green), and cellular nuclei (DAPI, in blue)
1152 is shown (**a**). Images were analyzed by confocal microscopy with a ×40/1.4 objective. Scale bars
1153 = 20 μm, (representative of n=2). Pearson's correlation (**b, d**) and Mander's overlap (**c, e**)
1154 coefficient derived from imaging experiments. Colocalization analysis of Z stacks was performed
1155 using the Colocalization module of Volocity from 3 to 8 separate Z-stacks. Individual numbers
1156 plotted display the corresponding values from each Z-stack for each Donor, error bars show the
1157 SEM. **(f, g)** hTECs infected as in panel A were stained for STING (in red), SARS-CoV-2 N (in
1158 green), and cellular nuclei (DAPI, in blue). Images (**f**) were analyzed by confocal microscopy with
1159 a ×20 objective. Scale bars = 50 μm, (representative of n=2). Colocalization analysis of Z stacks
1160 was performed as above and Pearson's correlation coefficient derived from 3 to 6 separate Z-
1161 stacks was plotted, error bars show SEM (**g**). (**h, i**) hTECs from three donors were pretreated with
1162 20 μM SN-011 or H-151 for 48h (both apical and basal chambers) and infected with SARS-CoV-
1163 2 mNG as above in the presence of compounds in the basal chamber. Virus release in the ALI
1164 chamber (**h**) and expression levels of the indicated ISGs (**i**) were analyzed by RT-qPCR. Data in
1165 (**h**) show the copies of cell-free SARS-CoV-2 N RNA in culture supernatants of compound-treated

1166 cells normalized relative to mock-treated samples. Data show the mean from n=2 independent
1167 biological replicates, error bars show SEM. Source data are provided as a Source Data file.

1168 **Figure 10. Expression profiles of cGAS, STING and representative ISGs in the healthy**
1169 **human airways.** Normalized counts and cell type metadata were downloaded from a publicly
1170 available single-cell study [94]. Detection frequency represents that percentage of cells with > 0
1171 counts for respective gene. Bar plots display the average normalized expression for a gene within
1172 a cell type. For the gene set representing the interferon alpha Gene Ontology term, normalized
1173 expression levels were summed for all genes in the set prior to computing detection frequencies
1174 and average expression.

1175

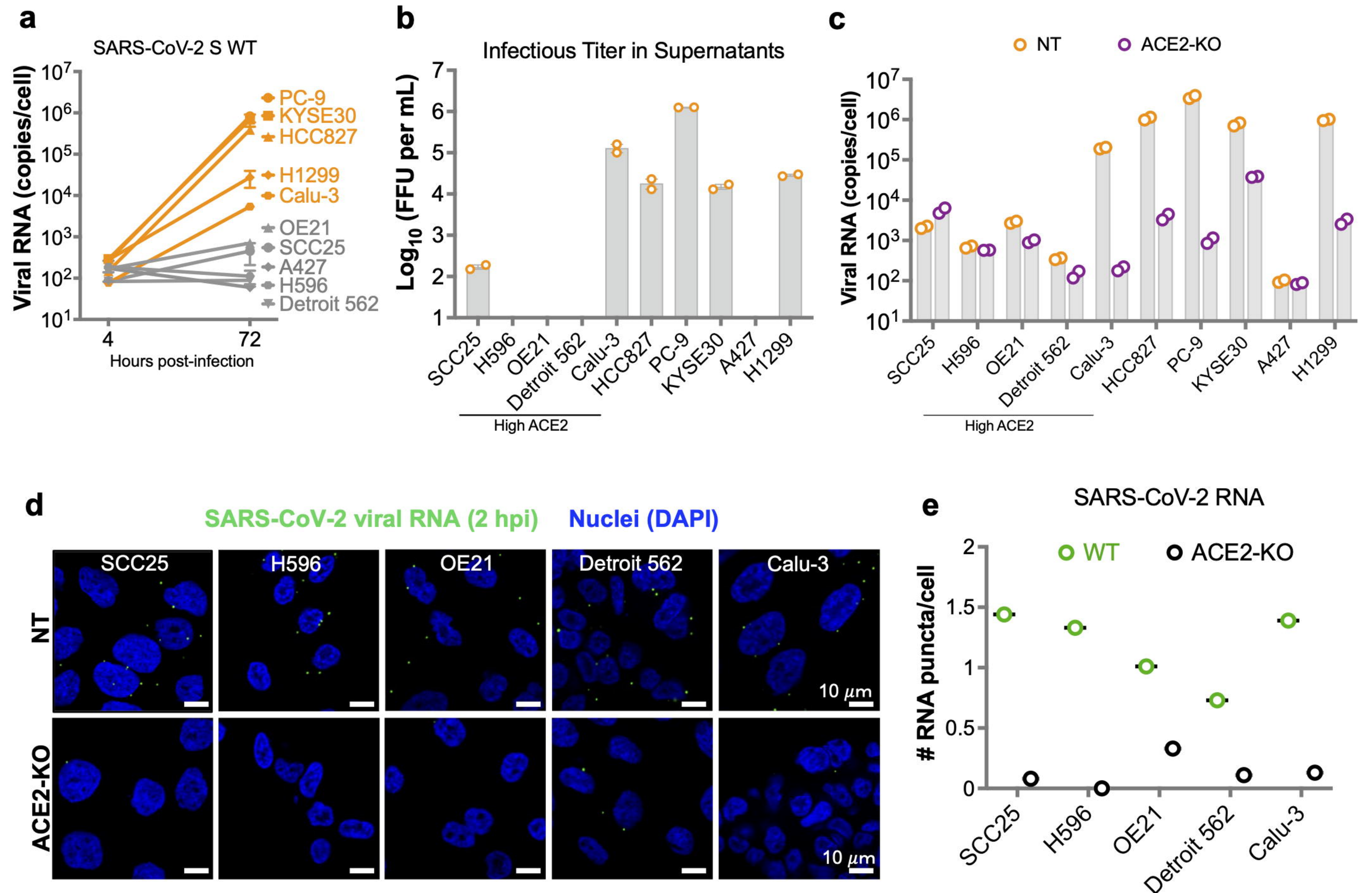
a
SARS-CoV-2 S WT
Viral RNA (copies/cell)
Hours post-infection
PC-9
KYSE30
HCC827
H1299
Calu-3
OE21
SCC25
A427
H596
Detroit 562
b
Infectious Titer in Supernatants
Log10 (FFU per mL)
High ACE2
c
NT
ACE2-KO
Viral RNA (copies/cell)
High ACE2
d
SARS-CoV-2 viral RNA (2 hpi)
Nuclei (DAPI)
SCC25
H596
OE21
Detroit 562
Calu-3
NT
ACE2-KO
10 μm
e
SARS-CoV-2 RNA
WT
ACE2-KO
RNA puncta/cell

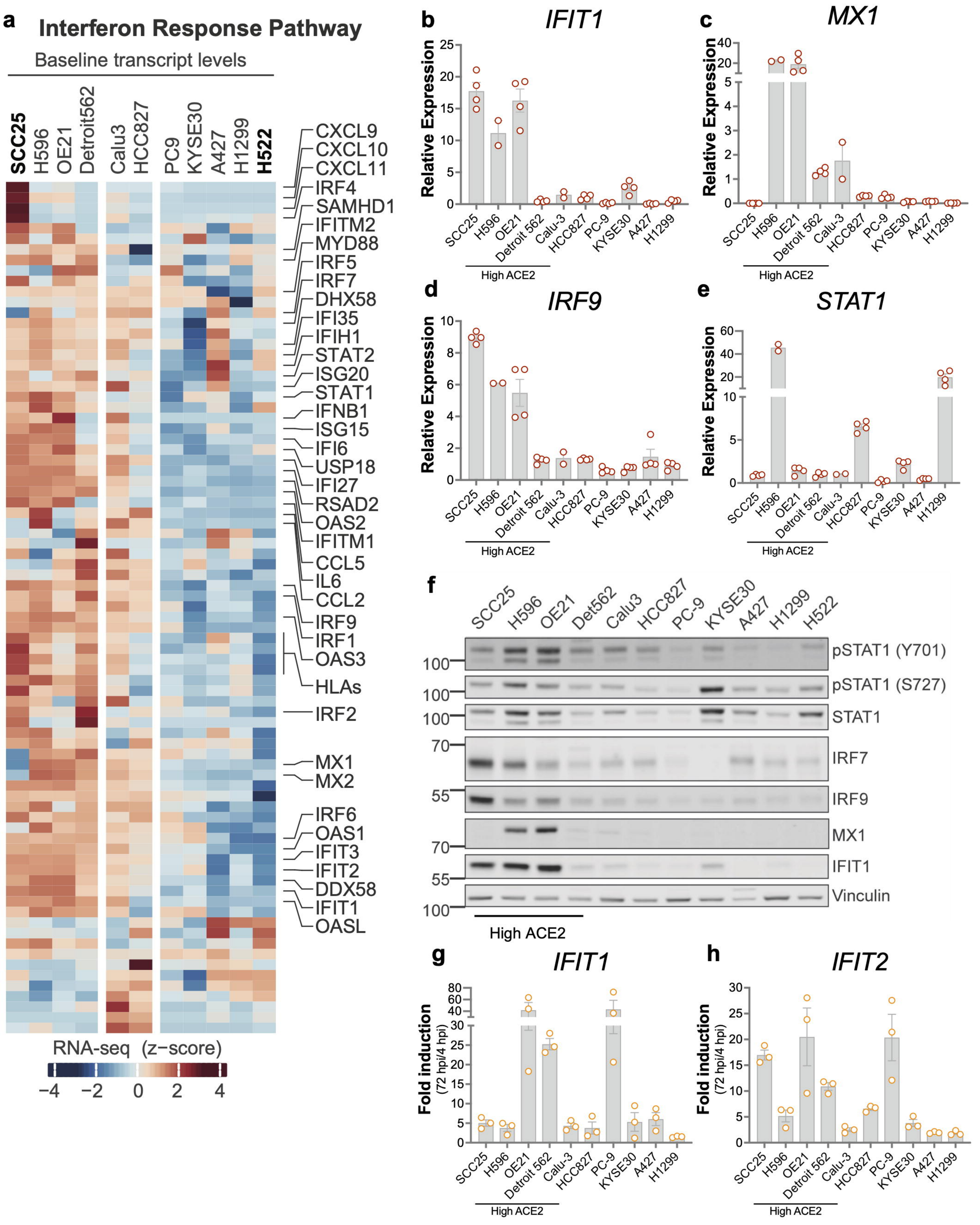
a
Interferon Response Pathway
Baseline transcript levels
SCC25
H596
OE21
Detroit562
Calu3
HCC827
PC9
KYSE30
A427
H1299
H522
CXCL9
CXCL10
CXCL11
IRF4
SAMHD1
IFITM2
MYD88
IRF5
IRF7
DHX58
IFI35
IFIH1
STAT2
ISG20
STAT1
IFNB1
ISG15
IFI6
USP18
IFI27
RSAD2
OAS2
IFITM1
CCL5
IL6
CCL2
IRF9
IRF1
OAS3
HLAs
IRF2
MX1
MX2
IRF6
OAS1
IFIT3
IFIT2
DDX58
IFIT1
OASL
RNA-seq (z−score)
−4 −2 0 2 4
b
IFIT1
c
MX1
d
IRF9
e
STAT1
Relative Expression
SCC25 H596 OE21 Detroit 562 Calu-3 HCC827 PC-9 KYSE30 A427 H1299
High ACE2
f
SCC25 H596 OE21 Det562 Calu3 HCC827 PC-9 KYSE30 A427 H1299 H522
pSTAT1 (Y701)
pSTAT1 (S727)
STAT1
IRF7
IRF9
MX1
IFIT1
Vinculin
100
70
55
High ACE2
g
IFIT1
h
IFIT2
Fold induction
(72 hpi/4 hpi)
SCC25 H596 OE21 Detroit 562 Calu-3 HCC827 PC-9 KYSE30 A427 H1299
High ACE2

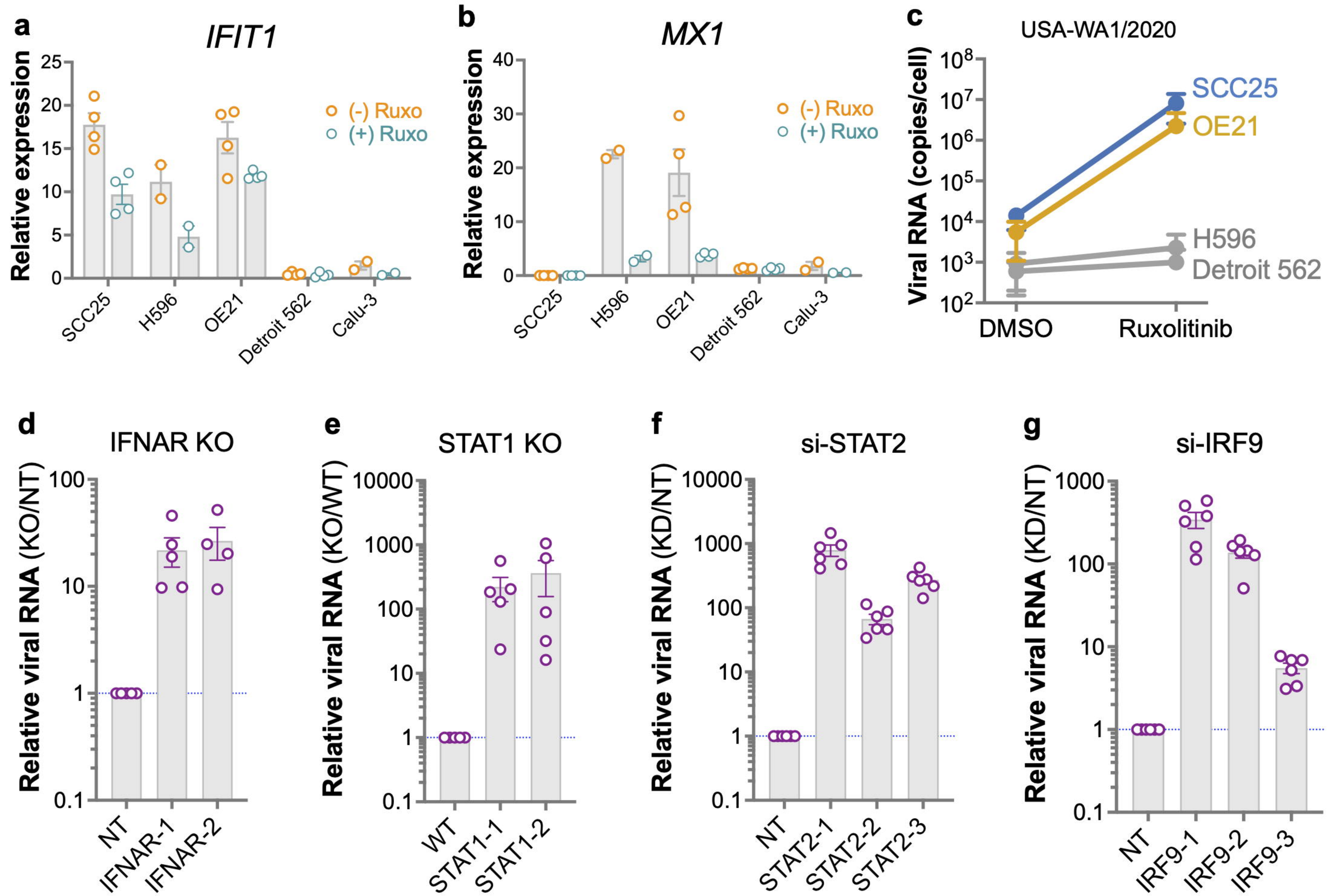
a
IFIT1
Relative expression
(-) Ruxo
(+) Ruxo
SCC25
H596
OE21
Detroit 562
Calu-3
b
MX1
Relative expression
(-) Ruxo
(+) Ruxo
SCC25
H596
OE21
Detroit 562
Calu-3
c
USA-WA1/2020
Viral RNA (copies/cell)
SCC25
OE21
H596
Detroit 562
DMSO
Ruxolitinib
d
IFNAR KO
Relative viral RNA (KO/NT)
NT
IFNAR-1
IFNAR-2
e
STAT1 KO
Relative viral RNA (KO/WT)
WT
STAT1-1
STAT1-2
f
si-STAT2
Relative viral RNA (KD/NT)
NT
STAT2-1
STAT2-2
STAT2-3
g
si-IRF9
Relative viral RNA (KD/NT)
NT
IRF9-1
IRF9-2
IRF9-3

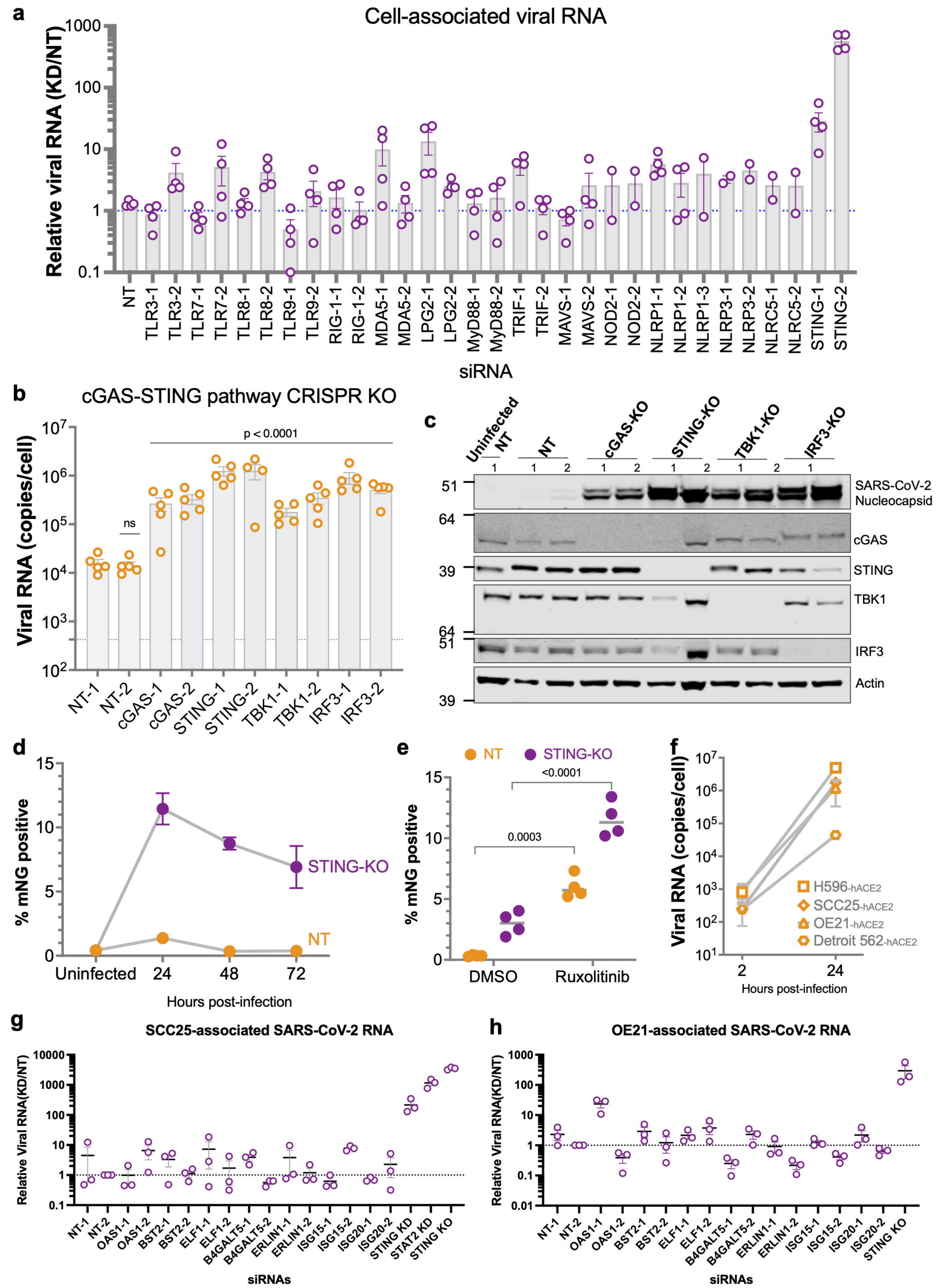
a
Cell-associated viral RNA
Relative viral RNA (KD/NT)
1000
100
10
1
0.1
NT
TLR3-1
TLR3-2
TLR7-1
TLR7-2
TLR8-1
TLR8-2
TLR9-1
TLR9-2
RIG-1-1
RIG-1-2
MDA5-1
MDA5-2
LPG2-1
LPG2-2
MyD88-1
MyD88-2
TRIF-1
TRIF-2
MAVS-1
MAVS-2
NOD2-1
NOD2-2
NLRP1-1
NLRP1-2
NLRP1-3
NLRP3-1
NLRP3-2
NLRC5-1
NLRC5-2
STING-1
STING-2
siRNA
b
cGAS-STING pathway CRISPR KO
Viral RNA (copies/cell)
10^7
10^6
10^5
10^4
10^3
10^2
p < 0.0001
ns
NT-1
NT-2
cGAS-1
cGAS-2
STING-1
STING-2
TBK1-1
TBK1-2
IRF3-1
IRF3-2
c
Uninfected
NT
NT
cGAS-KO
STING-KO
TBK1-KO
IRF3-KO
1
1
2
1
2
1
2
1
2
1
51
64
39
64
51
39
SARS-CoV-2 Nucleocapsid
cGAS
STING
TBK1
IRF3
Actin
d
% mNG positive
15
10
5
0
STING-KO
NT
Uninfected
24
48
72
Hours post-infection
e
NT
STING-KO
% mNG positive
15
10
5
0
<0.0001
0.0003
DMSO
Ruxolitinib
f
Viral RNA (copies/cell)
10^7
10^6
10^5
10^4
10^3
10^2
10^1
H596-hACE2
SCC25-hACE2
OE21-hACE2
Detroit 562-hACE2
2
24
Hours post-infection
g
SCC25-associated SARS-CoV-2 RNA
Relative Viral RNA(KD/NT)
10000
1000
100
10
1
0.1
NT-1
NT-2
OAS1-1
OAS1-2
BST2-1
BST2-2
ELF1-1
ELF1-2
B4GALT5-1
B4GALT5-2
ERLIN1-1
ERLIN1-2
ISG15-1
ISG15-2
ISG20-1
ISG20-2
STING KD
STAT2 KD
STING KO
siRNAs
h
OE21-associated SARS-CoV-2 RNA
Relative Viral RNA(KD/NT)
1000
100
10
1
0.1
0.01
NT-1
NT-2
OAS1-1
OAS1-2
BST2-1
BST2-2
ELF1-1
ELF1-2
B4GALT5-1
B4GALT5-2
ERLIN1-1
ERLIN1-2
ISG15-1
ISG15-2
ISG20-1
ISG20-2
STING KO
siRNAs

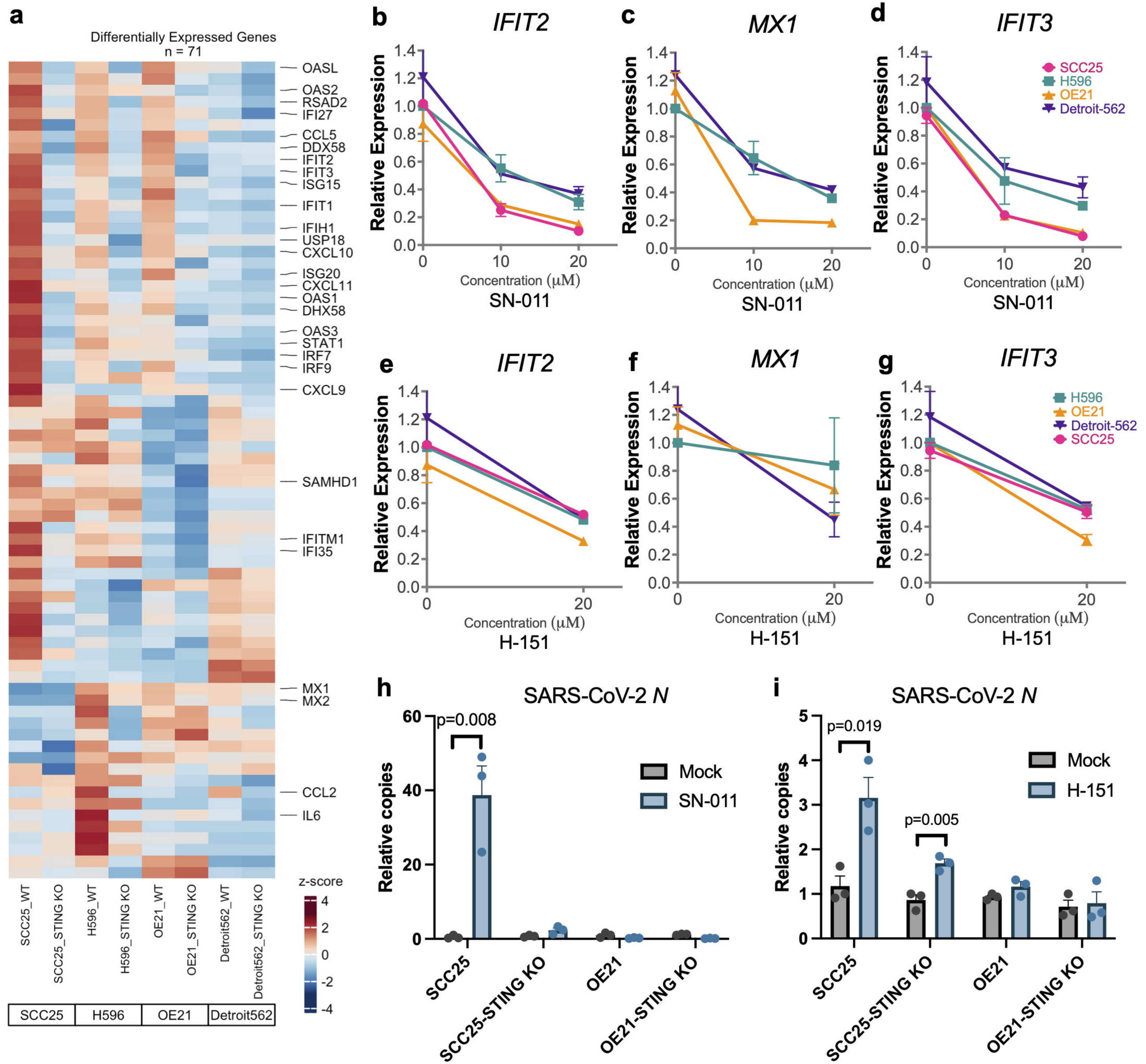
a
Differentially Expressed Genes
n = 71
OASL
OAS2
RSAD2
IFI27
CCL5
DDX58
IFIT2
IFIT3
ISG15
IFIT1
IFIH1
USP18
CXCL10
ISG20
CXCL11
OAS1
DHX58
OAS3
STAT1
IRF7
IRF9
CXCL9
SAMHD1
IFITM1
IFI35
MX1
MX2
CCL2
IL6
SCC25_WT
SCC25_STING KO
H596_WT
H596_STING KO
OE21_WT
OE21_STING KO
Detroit562_WT
Detroit562_STING KO
SCC25
H596
OE21
Detroit562
z-score
4
2
0
-2
-4
b
IFIT2
c
MX1
d
IFIT3
Relative Expression
Concentration (μM)
SN-011
SCC25
H596
OE21
Detroit-562
e
IFIT2
f
MX1
g
IFIT3
H-151
h
SARS-CoV-2 N
p=0.008
Relative copies
Mock
SN-011
SCC25
SCC25-STING KO
OE21
OE21-STING KO
i
SARS-CoV-2 N
p=0.019
p=0.005
Mock
H-151

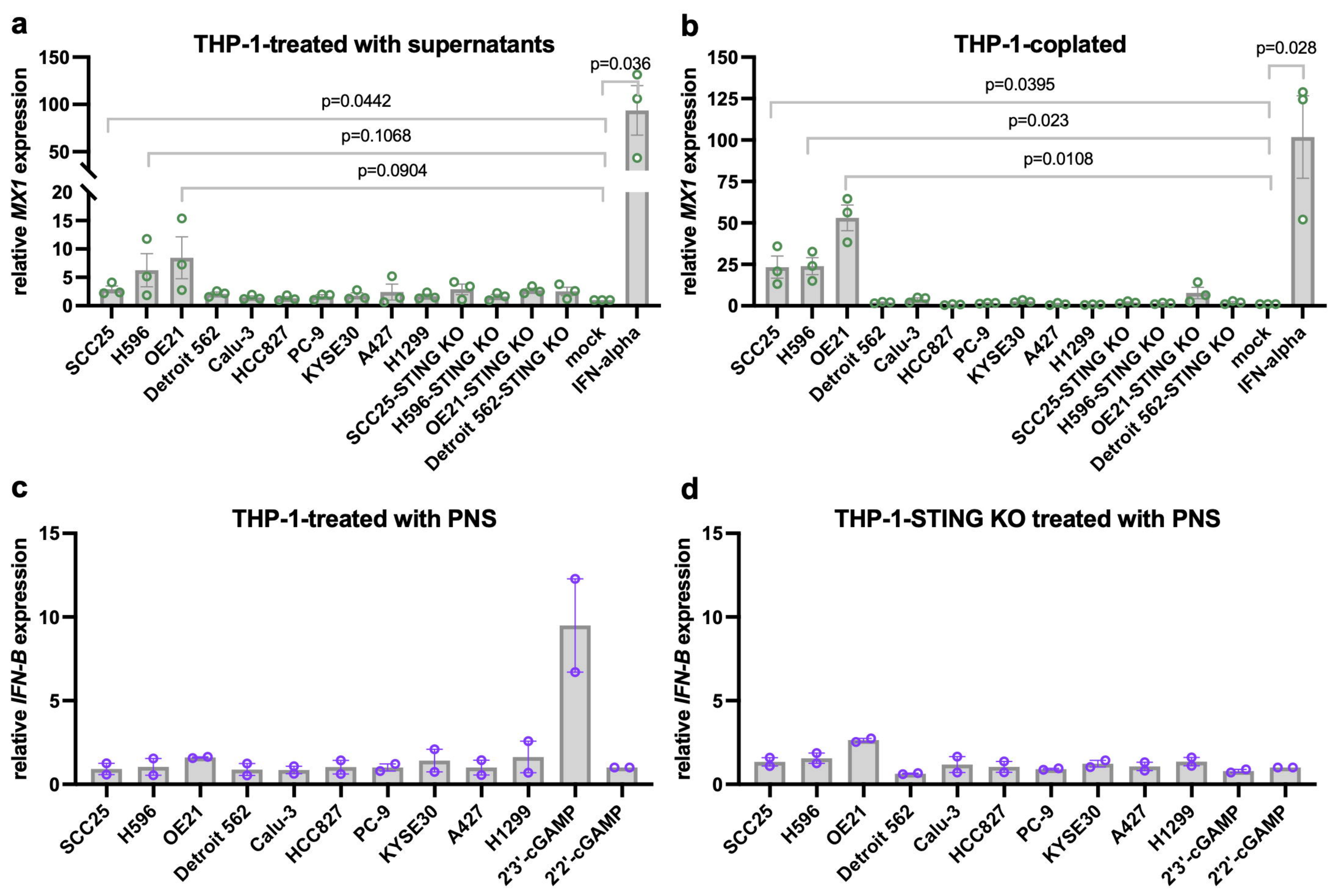
a
THP-1-treated with supernatants
relative MX1 expression
150
100
50
20
15
10
5
0
p=0.0442
p=0.1068
p=0.0904
p=0.036
SCC25
H596
OE21
Detroit 562
Calu-3
HCC827
PC-9
KYSE30
A427
H1299
SCC25-STING KO
H596-STING KO
OE21-STING KO
Detroit 562-STING KO
mock
IFN-alpha
b
THP-1-coplated
relative MX1 expression
150
125
100
75
50
25
0
p=0.0395
p=0.023
p=0.0108
p=0.028
SCC25
H596
OE21
Detroit 562
Calu-3
HCC827
PC-9
KYSE30
A427
H1299
SCC25-STING KO
H596-STING KO
OE21-STING KO
Detroit 562-STING KO
mock
IFN-alpha
c
THP-1-treated with PNS
relative IFN-B expression
15
10
5
0
SCC25
H596
OE21
Detroit 562
Calu-3
HCC827
PC-9
KYSE30
A427
H1299
2'3'-cGAMP
2'2'-cGAMP
d
THP-1-STING KO treated with PNS
relative IFN-B expression
15
10
5
0
SCC25
H596
OE21
Detroit 562
Calu-3
HCC827
PC-9
KYSE30
A427
H1299
2'3'-cGAMP
2'2'-cGAMP

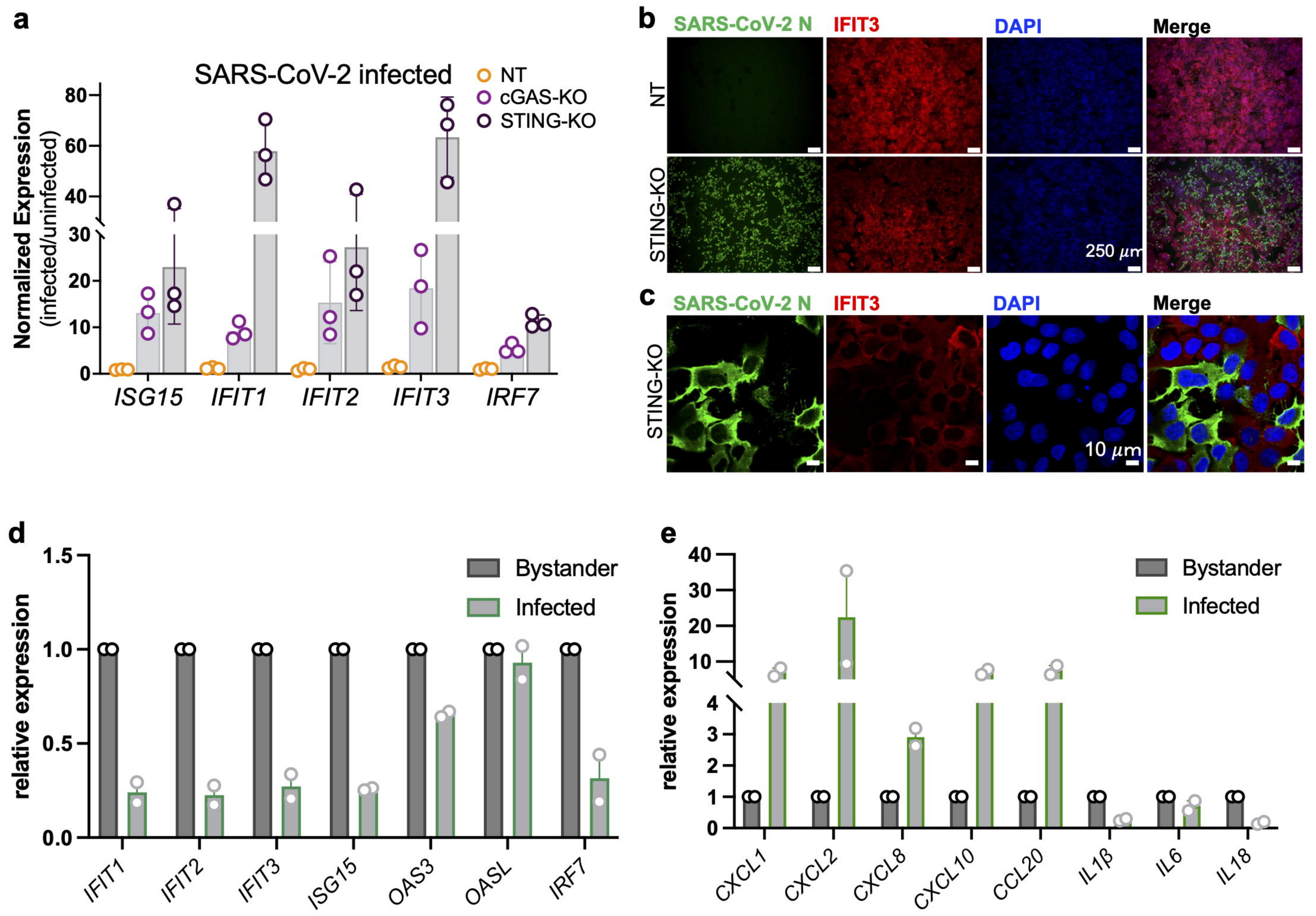
a
SARS-CoV-2 infected
NT
cGAS-KO
STING-KO
Normalized Expression
(infected/uninfected)
80
60
40
30
20
10
0
ISG15
IFIT1
IFIT2
IFIT3
IRF7
b
SARS-CoV-2 N
IFIT3
DAPI
Merge
NT
STING-KO
250 μm
c
SARS-CoV-2 N
IFIT3
DAPI
Merge
STING-KO
10 μm
d
Bystander
Infected
relative expression
1.5
1.0
0.5
0.0
IFIT1
IFIT2
IFIT3
ISG15
OAS3
OASL
IRF7
e
Bystander
Infected
relative expression
40
30
20
10
4
3
2
1
0
CXCL1
CXCL2
CXCL8
CXCL10
CCL20
IL1β
IL6
IL18

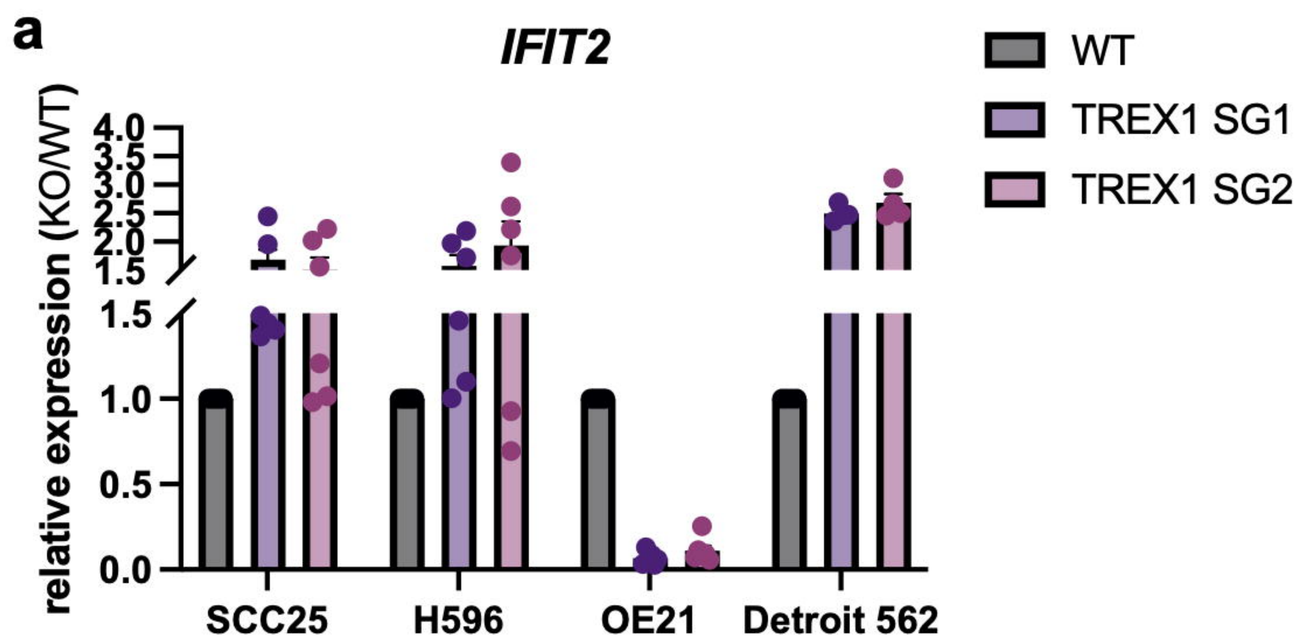

b

	SCC25	H596	OE21	Detroit 562
cGAS	-	T35N	-	T35N, P261H
STING	H232R	H232R	H232R	H232R

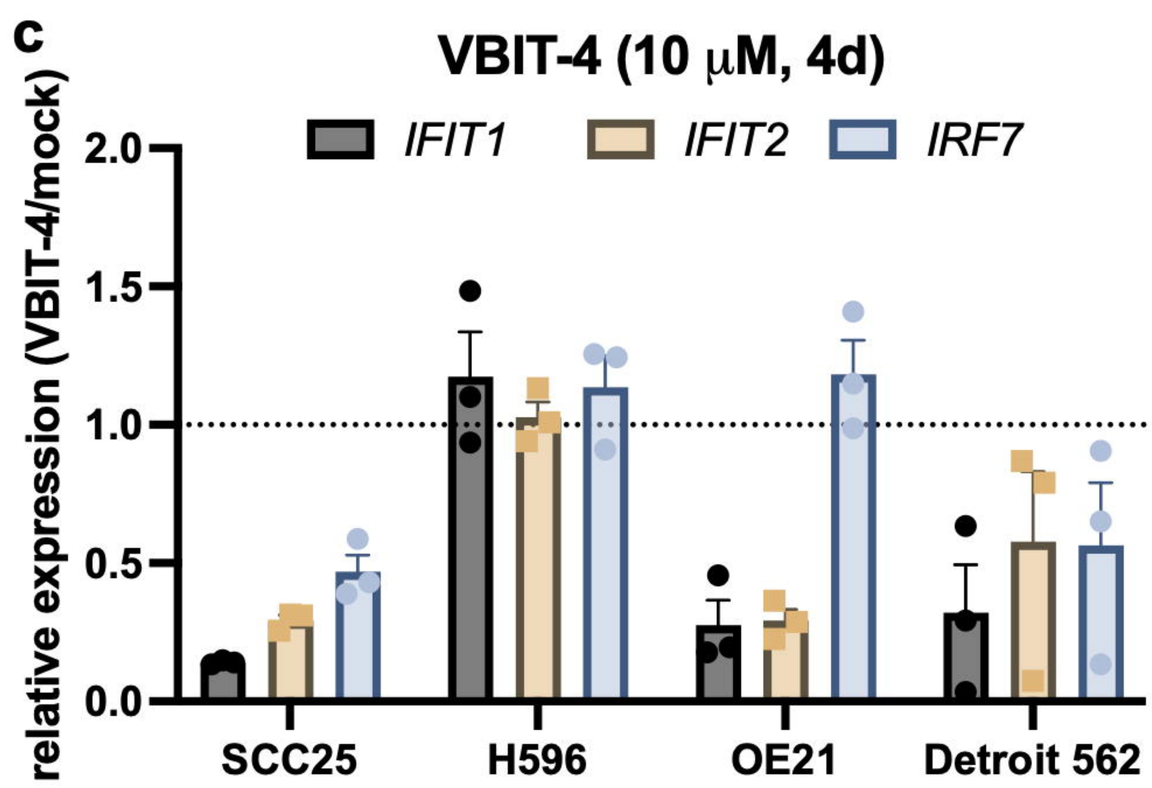

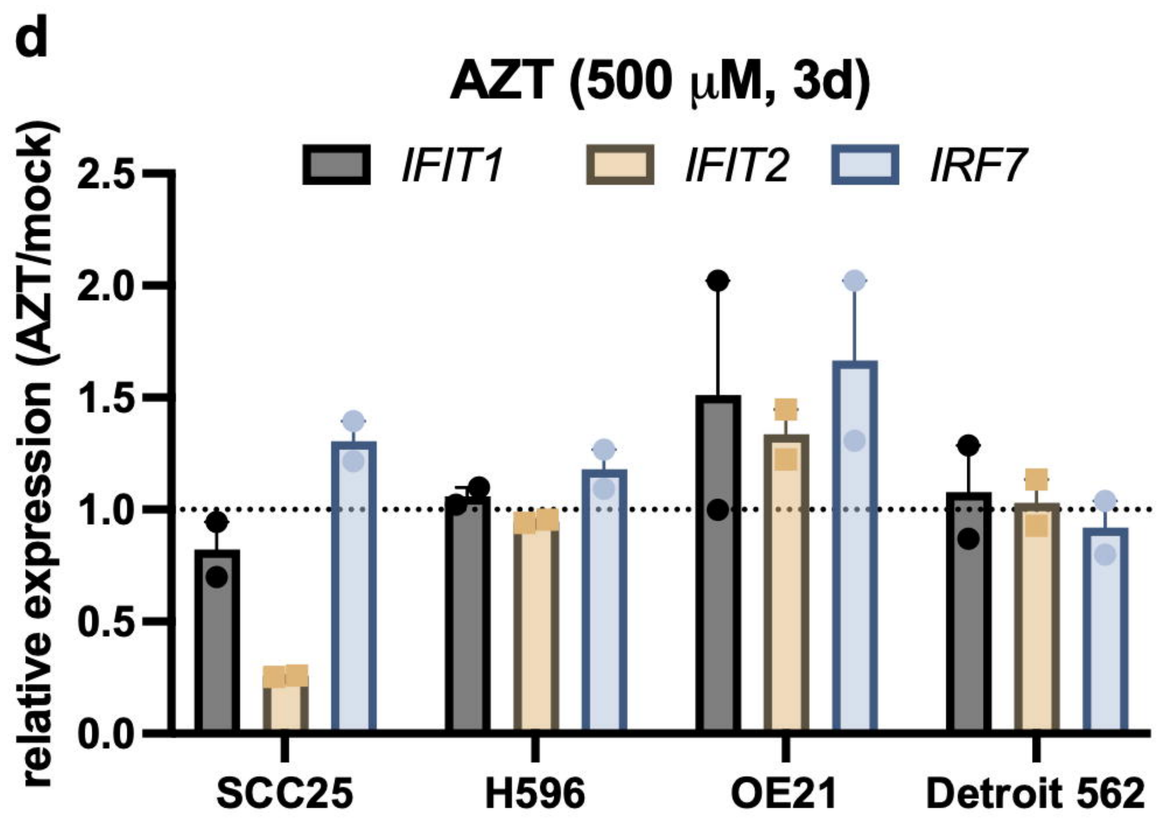

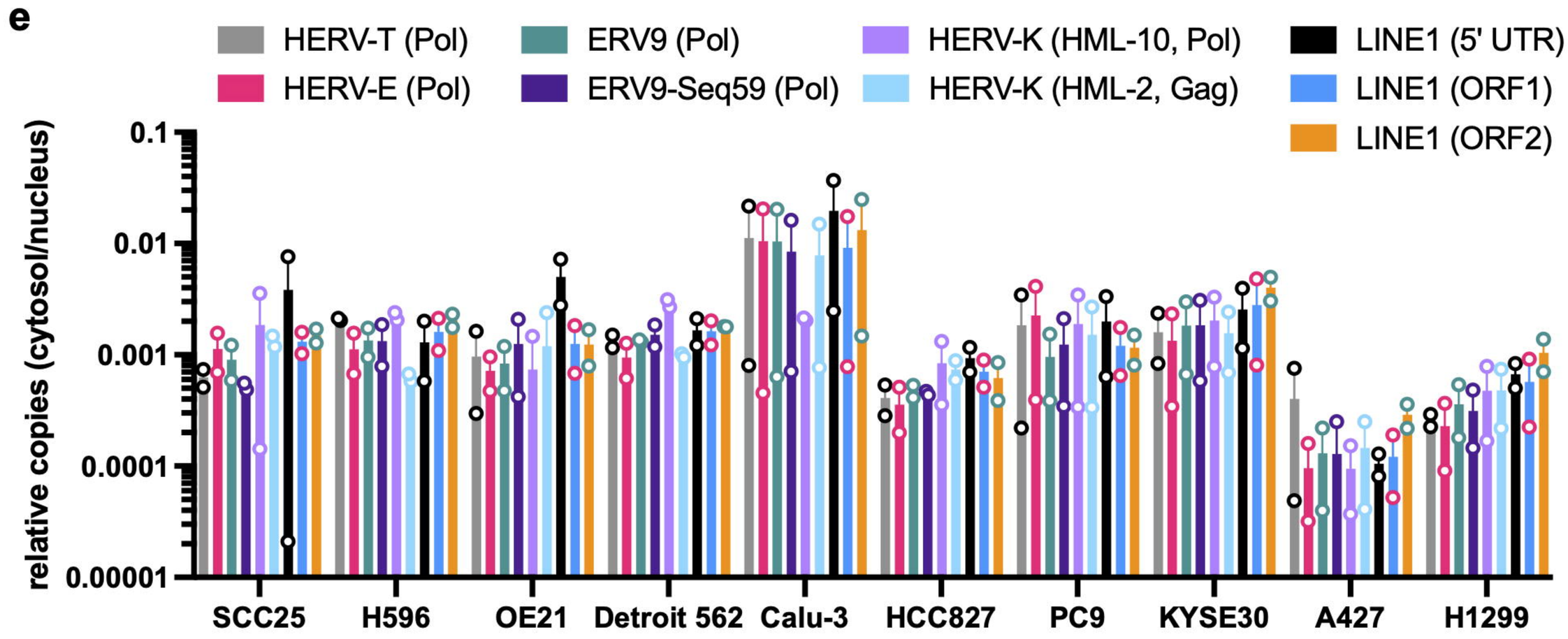

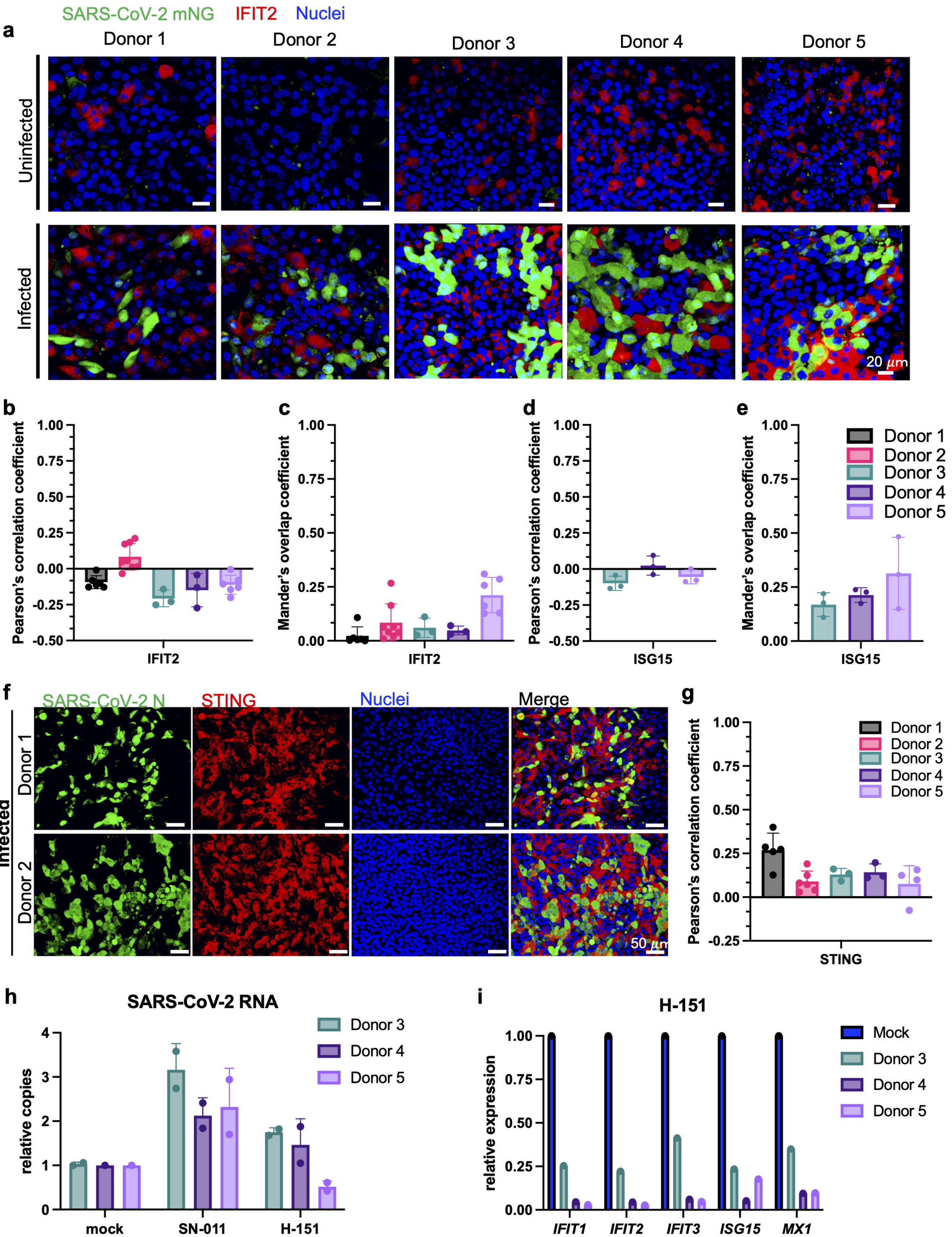
a
SARS-CoV-2 mNG
IFIT2
Nuclei
Donor 1
Donor 2
Donor 3
Donor 4
Donor 5
Uninfected
Infected
20 μm
b
Pearson's correlation coefficient
IFIT2
c
Mander's overlap coefficient
IFIT2
d
Pearson's correlation coefficient
ISG15
e
Mander's overlap coefficient
ISG15
Donor 1
Donor 2
Donor 3
Donor 4
Donor 5
f
SARS-CoV-2 N
STING
Nuclei
Merge
Infected
Donor 1
Donor 2
50 μm
g
Pearson's correlation coefficient
STING
h
SARS-CoV-2 RNA
relative copies
mock
SN-011
H-151
Donor 3
Donor 4
Donor 5
i
H-151
relative expression
IFIT1
IFIT2
IFIT3
ISG15
MX1
Mock
Donor 3
Donor 4
Donor 5

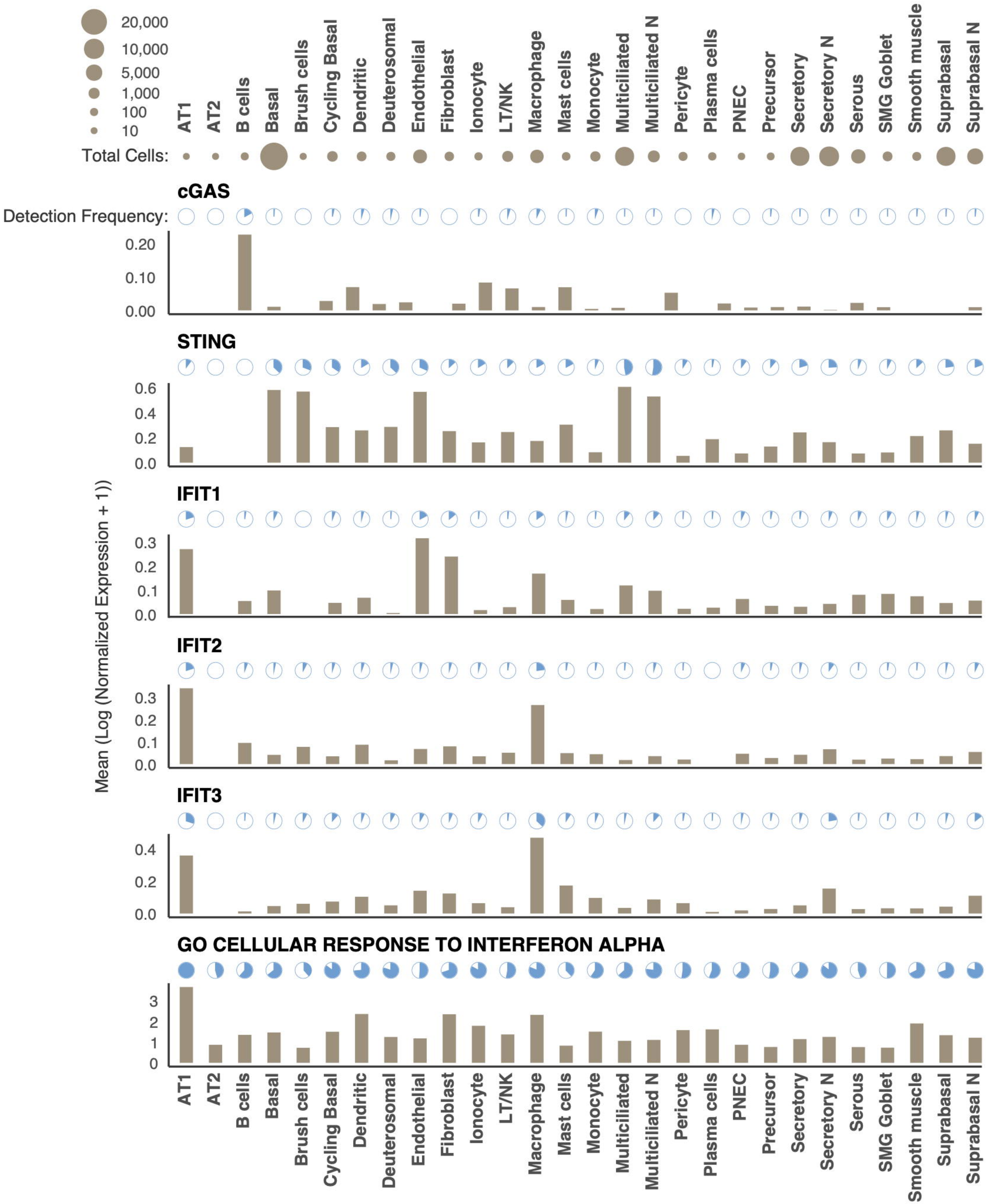
20,000
10,000
5,000
1,000
100
10
Total Cells:
AT1
AT2
B cells
Basal
Brush cells
Cycling Basal
Dendritic
Deuterosomal
Endothelial
Fibroblast
Ionocyte
LT/NK
Macrophage
Mast cells
Monocyte
Multiciliated
Multiciliated N
Pericyte
Plasma cells
PNEC
Precursor
Secretory
Secretory N
Serous
SMG Goblet
Smooth muscle
Suprabasal
Suprabasal N
cGAS
Detection Frequency:
0.20
0.10
0.00
STING
0.6
0.4
0.2
0.0
IFIT1
0.3
0.2
0.1
0.0
IFIT2
0.3
0.2
0.1
0.0
IFIT3
0.4
0.2
0.0
GO CELLULAR RESPONSE TO INTERFERON ALPHA
3
2
1
0
Mean (Log (Normalized Expression + 1))